Continuum Mech. Thermodyn. (2025) 37:59
https://doi.org/10.1007/s00161-025-01389-6

ORIGINAL ARTICLE

Chiara Pancella · Francesco D'Annibale

A Timoshenko-like equivalent beam model for the static analysis of a chiral metamaterial

Received: 8 February 2025 / Accepted: 7 April 2025 / Published online: 27 May 2025

Abstract In this paper, a one-dimensional Timoshenko-like equivalent beam model, embedded in a 2D space, is developed to analyze the static response of a chiral metamaterial, first presented in Misra et al. (Contin Mech Thermodyn 32:1497–1513, 2020). This is a beam-like structure, here referred to as the 'grain beam', which is made of a periodic assembly of a grain-pair interconnected with solid bars, exhibiting chirality through shear and axial strains coupling. The derivation of the beam model is conducted within the framework of the direct one-dimensional approach, wherein the constitutive law is established through a suitable homogenization procedure, that relies on an energy equivalence between a cell of the periodic model and a segment of the solid beam. Based on the geometry of the interconnecting elements of a grain-pair of the microstructure, analytical as well as numerical approaches are developed to identify the constitutive parameters, the latter grounded on a FE analysis of the cell. The analytical identification procedure, which shed the light on the dependence of the elastic coefficients upon proper defined nondimensional parameters, as the cell aspect ratio and the slenderness of horizontal and vertical fibers, is shown to be effective in designing grain beams with targeted stiffnesses, chirality and macroscopic behavior. The linear static response of some grain beams, taken as case studies, is analyzed and the results obtained by the Timoshenko-like beam model and the FE analyses, these latter carried out on refined models of grain beams, are compared. The effectiveness of the beam model, its limits of applicability, and the associated error magnitude in describing the static behavior of grain beams are investigated and discussed.

Keywords Equivalent beam model · Timoshenko beam · Chiral Metamaterials · Grain beam · Microstructured beam · Homogenization procedure

1 Introduction

In recent years, the focus in various applied sciences has been directed towards research on periodic microstructured systems, such as metamaterials and architected materials, a trend driven by notable advancements, on one side, in mathematically driven design, and on the other, on the feasibility of fabricating them through 3D printing methodologies, see, e.g., [1–10]. From an engineering point of view, microstructured bodies are able

C. Pancella · F. D'Annibale (✉)
Department of Civil, Construction-Architectural and Environmental Engineering, University of L'Aquila, 67100 L'Aquila, Italy
E-mail: francesco.dannibale@univaq.it

C. Pancella
E-mail: chiara.pancella@graduate.univaq.it

F. D'Annibale
International Research Center on Mathematics and Mechanics of Complex Systems, 67100 L'Aquila, Italy

to exhibit exceptional characteristics surpassing those of traditional bulk materials in aspects such as weight, including enhanced mechanical performance, resilience, impact resistance, and overall energy absorption capability (see, e.g. [9–15]).

Among the others, some metamaterials, that cannot be superimposed on their mirror image, are known as chiral metamaterials, since they exhibit the property of chirality. Two-dimensional chiral metamaterials, see, e.g., [16–20], can be used to achieve mechanical anisotropy, as in [16], and an auxetic behavior with a negative Poisson's ratio, as in [17,18], and also to balance bending loads through tensile loads, as in [19]. For example, in [18], a chiral honeycomb metamaterial, representative of four distinct classes of 2D Euclidean tessellations with hexagonal rotational symmetry, is designed to obtain a new auxetic material. In [19], a tetrachiral unit-cell is studied to demonstrate that the coupling of normal and shear deformations can be used as a primal loadbalancing mechanism. The developed analytical model has been validated through both numerical simulations and experiments. In [20], the chirality in 2D Cosserat-like micromorphic continua is examined, establishing a connection with grain-scale mechanics through the Granular Micromechanics Approach (GMA). The study emphasizes the fact that additional kinematical descriptors are needed in modeling granular materials in order to properly describe grain-relative displacements. Also three-dimensional chiral metamaterials have been extensively studied in the literature, see, e.g., [21–24]. In [21], a gammadion-shaped chiral comprising inclined ligaments was incorporated into the chiral structure to achieve high torsional compliance. In [22], 3D chiral and achiral mechanical metamaterial were designed extending the 2D 'missing-rib' type of chiral cell to 3D with spherical tiling. The chiral design showed the compression-twisting coupling while the achiral design showed an auxetic behavior. In [23], the buckling strength of the chiral lattice columns, constructed by periodically placing the inclined straight beams in a chiral manner, which exhibit compression-twisting coupling effect, was studied. Its deformation was described with a constitutive model based on the Cosserat rod theory and, with the semi-analytical homogenization method proposed, the effects of chirality on the buckling strength and buckling mode were revealed. In [24], panto-cylinders, whose microstructure consists of two families of helicoidal beams interconnected by perfect or elastic joints, were studied using a numerical integration strategy to determine the deformation shapes of Cosserat rods in order to predict their behavior. Numerical simulations were conducted to investigate the mechanical parameters that emphasize the chirality effects and chiral deformation patterns, both depending on the type of joint and its length.

Numerical approaches, such as those based on Finite-Element Method, are very important for the detailed design and analysis of periodic structures (see, e.g., [25]), nevertheless, there is a growing interest in the literature in getting simple models via homogenization techniques (see, e.g., [26–29] and the recent reviews [30,31]). In fact, these equivalent models (i) require, in general, a lower computational effort to solve the elastic problem with respect to correspondent finite-element ones, (ii) offer interpretive advantages compared to purely numerical modeling in terms of structural global behavior, and, even more important, (iii) closed-form solutions can be pursued in several problems of engineering interest, such as static, dynamic and buckling analyses of periodic structures. In those cases where one dimension of the microstructured body predominates over the other two, homogenization facilitates the derivation of a beam-like model of the periodic structure at hand.

Among the different homogenization approaches existing in the literature to obtain the equivalent beam model, a so-called 'mixed approach' has been developed and applied in dealing with statics, dynamics, buckling and aeroelasticity of periodic (planar and three-dimensional) frame structures, such as microstructured grid cylinders [32–35], buildings and towers [36–44]. The mixed approach combines the heuristic (see, e.g. [45,46]) and asymptotic (see, e.g., [47–51]) homogenization approaches, since the continuum model is heuristically predicted (not analytically derived as in the latter), but the micro–macro relationships, needed for the up-scaling procedure, that is the constitutive behavior, are analytically determined (not predicted as in the former) on the ground of energy equivalence between a cell of the periodic system and a segment of the continuous beam, that can be carried out within an analytical or a numerical framework, depending on the complexity of the microstructure at hand (see, e.g., [32,33,52]). In these papers, shear beam models, also including torsional effect in the three-dimensional (3D) behavior, as well as Timoshenko beam models have been formulated, by identifying the floors and the columns of the periodic frames, with the cross-sections and longitudinal fibers of the continuous beam, respectively, and by introducing some strong hypotheses, separately or in combination, regarding, in particular: in-plane (membrane) and out-of-plane (flexural) undeformability of the cross-sections and inextensibility of the longitudinal fibers. When all these hypotheses are considered, the equivalent model is as a shear-(shear-torsional) beam in a 2-(3)D space; when the extensibility of the longitudinal fibers is taken into account, the equivalent model is a Timoshenko beam. Moreover, in [32–34,44], the cross-section's undeformability has been reduced, considering out-of-plane deformability, specifically the warping of the cross-sections, through the concepts of ‘shear factor’ and ‘flexural factor’. In essence, even when heuristically employing a rigid cross-section beam model, some corrective factors are suitably introduced to better estimate the shear and flexural stiffness of the homogenized beam: this is achieved by incorporating, on an energetic balance (that, again, can be carried out either analytically or numerically, depending on the microstructure complexity), the effect of the neglected warping, akin to the approach taken to incorporate the de Saint-Venant’s Theory results into the Timoshenko Beam’s Theory.

Within the periodic structures of interest in the present work, in [1,2], a specific microstructure has been conceived as the mechanical (rheological) analog of the peculiar interaction of a granular material that is composed by a set of solid bars connecting two grains. It is has been also shown that, thanks to its particular geometry, the granular material exhibit the property of chirality. In [2], a non-standard Timoshenko beam model for such a chiral metamaterial, is proposed; accordingly, a numerical procedure, which is grounded on a Finite-Element modeling of the whole periodic structure, is applied for the identification of the constants of the constitutive matrix of the equivalent beam model. The procedure involves solving three distinct types of planar equilibrium problems, referred to as identification tests. The selection of these identification tests, and thus the choice of boundary and load conditions, derives from the necessity to engage a subset of the stiffnesses enabled by the specific microstructure. Simulations were conducted using a 2D Cauchy continuum, with the left and right boundary grains treated as rigid domains. It is worth to notice that the microstructure of [2] is of scientific interest because its behavior reveals common tracts also with mechanical cable models or the analysis of DNA filaments [53–55]. In the literature, numerous microstructures based on chiral geometry exist, each exploring various connections between adjacent cells distinct from the one studied in [2]. As an example, in [56], where the study object is a duoskelion structure, introduced as a discrete spring model, a specific scaling law for micro stiffnesses it’s been selected aimed at deriving, via asymptotic homogenization, an internally-constrained Cosserat one-dimensional planar continuum model as the limit of a duoskelion structure. However, duoskelion structures have been studied not only in static but also by analyzing their response to in-plane dynamic instability problems, as in [57]. Also structures, obtained through the assembly of duoskelion beams are addressed in the literature, as in [58], in which the microstructure is characterized by the connection of two orthogonal families of parallel equispaced duoskelion beams.

Furthermore, other approaches, including experimental ones, have also been developed in [1,3,4,59] to analyze the behavior of the chiral microstructure similar to that of [2]. In [1], the Granular Micromechanics Approach (GMA) has been applied to predict the closed-form expressions for elastic constants of a macroscale 2D chiral granular metamaterial. The latter was designed with a grain-pair interaction in order to exhibit shear-normal-rotational coupling. The coupling prediction was confirmed thanks to tensile experiments conducted on specimens realized through additive manufacturing (3D printing). In [3], Digital Image Correlation (DIC) was carried out on specimens fabricated using 3D printing and tested in an uniaxial testing machine. The designed structures were representative of granular metamaterial composed of rigid grains interacting with each other through grain-pair interaction mechanisms. The repeatability of the measurement was demonstrated and the range of validity of the derived model was assessed by calibration. In this regard, results showed that the calculations matched the measured deformations only at small strain level. In fact, the higher the strain level, the more material and geometrical nonlinearities become significant and thus, due to the effect of boundary layer and nonlinear interactions between grains, some differences from the calculated responses were observed. In [4], a multiscalar DIC methodology was employed, beginning with a macroscale observation of the problem (where the microstructure is overlooked and the construct is treated as a continuum bar), followed by an exploration of the underlying microstructure through microscale DIC analysis. The microscale results revealed that the granular material consists of a collection of nearly rigid grains that store elastic energy through intergranular mechanisms. Moreover, the analyses demonstrated that, under extension, non-standard deformation mechanisms, including grain rotations, occur, and that the transverse displacements of the grains are governed by the behavior of the grain interconnections. Furthermore, it is worth to notice that, in the design and analysis of metamaterials built up with additive manufacturing processes, it is essential to account for the internal structure at the microscale, which, indeed, influences the overall mechanical response at the macroscale. To address this, in [60] a computational scheme applicable to a wide class of substructures is developed to identify metamaterial parameters by utilizing both macroscopic and microscopic scales. This approach is applied to a honeycomb substructure, considering the infill ratio. The parameters identified are related to the mechanical response of the metamaterials, such as elastic behavior and higher-order terms introduced by the substructure.

In this paper, microstructured bodies very similar to those analyzed in [1–4] are considered again. The mixed homogenization approach so far carried out for other microstructured metamaterials is applied here to obtain a Timoshenko-like homogenized beam model (coarse equivalent model), able to describe the linear static and planar behavior of such beam-like structures, here referred to as 'grain beams' (fine model). To identify the constitutive matrix of the equivalent model, two kinds of different assumptions have been made, grounded on the geometry of the grain pairs' interconnecting elements and the deformability of the grains, constituting the (fine) microstructure of the cell, and their relevant modeling, namely: (i) grains are modeled as rigid bodies, which are interconnected by deformable Timoshenko micro-beams, thus leading to an analytical identification of the constitutive matrix; (ii) both grains and interconnecting elements are modeled as 2D Cauchy continuum bodies, leading to a numerical identification of the relevant constitutive matrix. A qualitative analysis, based on an analytical identification procedure, has highlighted the dependence of elastic coefficients on suitably defined nondimensional parameters, such as the cell aspect ratio and the slenderness of horizontal and vertical fibers. This opens up new possibilities for designing the microstructure of granular beams to achieve a desired macroscopic response. Then, the linear static response of some grain beams, with different microstructures' geometry, taken as case studies, is analyzed to show the effectiveness and the limits of applicability of the coarse homogenized beam model. Numerical results obtained by the equivalent model are compared with Finite-Element (FE) analyses on planar grain beams, modeled with both beam and plate elements, in order to show the order of magnitude of the errors in the homogenization procedure.

The paper is organized as follows. In Sect. 2, the equations of the Timoshenko beam model, embedded in a 2D space, are recalled. In Sect. 3, the identification procedures are described. In Sect. 4, a qualitative analysis of the mechanical behavior of the microstructure is carried out. In Sect. 5, the comparisons between results provided by Finite-Element models of grain beams and the equivalent Timoshenko-like model, are developed. In Sect. 6, some conclusions and perspectives are drawn. Finally, the Appendix A, containing the analytical expression of the constitutive matrices, and the Appendix B, containing the analytical (exact) solution for the boundary value problem, close the paper.

2 The model

The microstructured body here considered is made of a periodic and specifically designed granular microstructure, i.e. the cell, depicted in Fig. 1. When such a microstructure, comprised between the grains i and $i+1$ is repeated n times in the x-direction (horizontal direction), as shown in Fig. 2a, the here referred to as 'grain beam' is obtained. The cell in Fig. 1 is referred to a (local) cartesian coordinate system $\tilde{O}\tilde{x}\tilde{y}$, originating at the centroid of the left grain $\tilde{O}$; it has a length h and it is composed of two semicircular half grains, of radius R, which are connected by two families of (micro) bodies, also referred to as 'fibers' throughout the paper, whose axis-lines are dashed in the figure, namely: (i) those parallel to the (local) $\tilde{x}$-axis of the cell, i.e. the horizontal fibers, and (ii) that parallel to the (local) $\tilde{y}$-axis of the cell, i.e. the vertical one. The width of the horizontal and vertical bodies is taken equal to t_ν $(\nu = x,\ y)$ where the subscript refers to the $\nu-$axis orientation ($x-$ or $y-$parallel); furthermore, the thickness of the cell, i.e. its dimension along the z-axis, not depicted in Fig. 1, is set to t_z for all the fibers, and assumed to be negligible with respect to cell length and height. As a consequence, a predominantly plane stress behavior occurs when in-plane loads are applied to the cell. Finally, the length ℓ_c denotes the distance between the vertical diameter of the grain and the intersection between the grain's circumference and the intrados or extrados of horizontal fibers. Accordingly, the length of the horizontal fibers, namely ℓ_x, results to be $\ell_x = h/2 - \ell_c$, while that of the vertical fiber is denoted as ℓ_y, both referred to their axis-lines.

It's important to remark that the cell lacks symmetry axes, thus resulting in some strains coupling at the macro-scale, the type of which depends on the microstructure's design. In particular, as discussed in [1,2], if the horizontal fibers have the same cross-sections, even if it is different from that of the vertical one, only shear-axial strains coupling occurs at the macro-scale, independently on the lengths ℓ_x and ℓ_y; on the other hand, if the horizontal fibers have different cross-sections (or lengths), independently on the length and cross-section of the vertical one, also the other couplings arise at the macro-level, such as axial-flexural and shear-flexural strains coupling. In what follows, the general cases $\ell_x \neq \ell_y$ and $t_x \neq t_y$ will be considered in the identification of the homogenized (equivalent) beam model, while numerical analyses will be carried out assuming $t_x = t_y =: t$. Therefore, only the coupling between shear and axial strains will be observed.

Furthermore, the grain beam is build up, as shown in Fig. 2a, where the (local and global) horizontal axes are taken coincident, namely $\tilde{x} \equiv x$, the origin O of the global coordinate system is assumed to be located on the $i = 0$ grain and, accordingly the local axis $\tilde{y}$ is parallel to y-axis, for each cell. In order to describe the statics of the grain beam, a one-dimensional continuum model, internally unconstrained, is heuristically adopted as

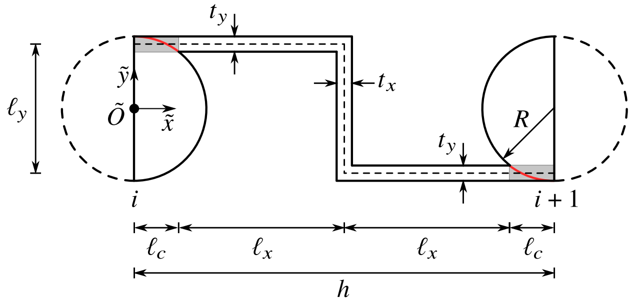

Fig. 1 Periodic microstructure of the grain beam

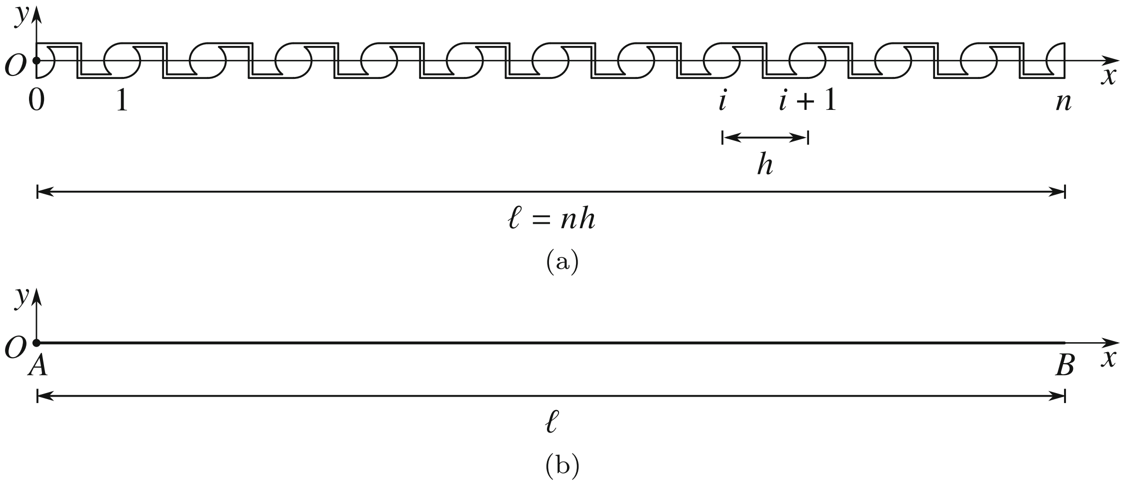

Fig. 2 Study object: **a** grain beam; **b** equivalent beam model

the target (and coarse) model, of the (fine) grain beam, according to the mixed homogenization approach. This is the well-known Timoshenko beam in linear kinematics, that is here modeled as a one-dimensional, polar continuum, embedded in a bi-dimensional space, (see, e.g. [61–64]). An initially straight beam is considered, having rigid cross-sections, orthogonal to the axis-line in the reference rectilinear configuration, and flexible axis-line. The beam is shown in Fig. 2b and it is referred to the material abscissa $x \in [0, \ell]$, spanning the point of the axis-line in the interval (A, B) of length $\ell := n\,h$.

Once the target model is introduced, kinematics and equilibrium are defined, while leaving the constitutive law unrestricted. Consequently, under the assumptions of the linear theory, i.e. for small displacements and strains, the following well-known strain–displacement relationships hold:

$$\begin{aligned} \varepsilon &= u', \\ \gamma &= v' - \theta, \\ \kappa &= \theta', \end{aligned} \tag{1}$$

which link the longitudinal displacement $u\,(x)$, the transverse displacement $v\,(x)$, and the rotation of the cross-section $\theta\,(x)$, to the elongation $\varepsilon\,(x)$, the shear strain $\gamma\,(x)$, and the flexural curvature $\kappa\,(x)$; here and in what follows, a prime denotes derivation with respect to the (independent) spatial variable. Without loss of generality, a double-clamped beam, fixed at the end A and subject to assigned displacements at end B, is considered for further analyses. Accordingly, the following geometric boundary conditions hold (the overbar denotes a prescribed quantity):

$$\begin{aligned} &u_A = 0, \quad v_A = 0, \quad \theta_A = 0, \\ &u_B = \bar{u}, \quad v_B = \bar{v}, \quad \theta_B = \bar{\theta}. \end{aligned} \tag{2}$$

The equilibrium is governed by the following well-known equations:

$$\begin{aligned} N' + p_x &= 0, \\ T' + p_y &= 0, \\ M' + T + c &= 0, \end{aligned} \tag{3}$$

where $N(x)$ and $T(x)$ are the axial and shear internal forces, respectively, $M(x)$ is the bending moment, $p_x(x)$, $p_y(x)$, $c(x)$ are the external forces and couple per unit-length.

It is assumed that the constitutive behavior of the beam is ruled by a linear elastic law; accordingly, the existence of a strain energy function, quadratic in the strain measures, is postulated, namely:

$$\phi(\varepsilon, \gamma, \kappa) = \frac{1}{2}\left[c_{11}\,\varepsilon^2 + c_{22}\,\gamma^2 + c_{33}\,\kappa^2 + 2\left(c_{12}\,\varepsilon\,\gamma\; + c_{13}\,\varepsilon\,\kappa\; + c_{23}\,\gamma\,\kappa\right)\right], \tag{4}$$

which depends on the six elastic constants c_{ij} $(i, j = 1, 2, 3)$, to be properly identified in order to effectively describe the macroscopic behavior of the granular microstructure. Therefore, according to the Green law:

$$\begin{aligned} N &= \frac{\partial \phi}{\partial \varepsilon}, \\ T &= \frac{\partial \phi}{\partial \gamma}, \\ M &= \frac{\partial \phi}{\partial \kappa}, \end{aligned} \tag{5}$$

a fully-coupled constitutive law is obtained. It reads:

$$\begin{pmatrix} N \\ T \\ M \end{pmatrix} = \begin{pmatrix} c_{11} & c_{12} & c_{13} \\ c_{12} & c_{22} & c_{23} \\ c_{13} & c_{23} & c_{33} \end{pmatrix} \begin{pmatrix} \varepsilon \\ \gamma \\ \kappa \end{pmatrix}, \tag{6}$$

in which:

$$\mathbf{C} := \begin{pmatrix} c_{11} & c_{12} & c_{13} \\ c_{12} & c_{22} & c_{23} \\ c_{13} & c_{23} & c_{33} \end{pmatrix}, \tag{7}$$

is the constitutive matrix. Then, once the equilibrium equations, Eq. (3), are written in terms of displacements by using Eqs. (6) and (1), the following elasto-static problem is obtained:

$$\begin{aligned} c_{11}u'' + c_{12}\left(v'' - \theta'\right) + c_{13}\theta'' + p_x &= 0, \\ c_{12}u'' + c_{22}\left(v'' - \theta'\right) + c_{23}\theta'' + p_y &= 0, \\ c_{13}u'' + c_{23}\left(v'' - \theta'\right) + c_{33}\theta'' + c_{12}u' + c_{22}\left(v' - \theta\right) + c_{23}\theta' + c &= 0. \end{aligned} \tag{8}$$

Equations (8) constitute a system of second-order partial differential equations, in the unknown displacement field, sided by the geometric boundary conditions Eq. (2). They admit a closed-form solution, as discussed, e.g., in [33] and in the Appendix B for the case of interest in the present paper.

Finally, when Eq. (8) and Eq. (2) are recast in matrix form, they reads:

$$\begin{aligned} \mathbf{K}_2\mathbf{u}'' + \mathbf{K}_1\mathbf{u}' + \mathbf{K}_0\mathbf{u} + \mathbf{p} &= \mathbf{0}, \\ \mathbf{u}_A &= \mathbf{0}, \\ \mathbf{u}_B &= \bar{\mathbf{u}}_B, \end{aligned} \tag{9}$$

where:

$$\begin{gathered} \mathbf{u} := \begin{pmatrix} u \\ v \\ \theta \end{pmatrix}, \qquad \mathbf{p} := \begin{pmatrix} p_x \\ p_y \\ c \end{pmatrix}, \qquad \bar{\mathbf{u}}_B := \begin{pmatrix} \bar{u} \\ \bar{v} \\ \bar{\theta} \end{pmatrix}, \\ \mathbf{K}_2 := \begin{pmatrix} c_{11} & c_{12} & c_{13} \\ c_{12} & c_{22} & c_{23} \\ c_{13} & c_{23} & c_{33} \end{pmatrix} \equiv \mathbf{C}, \quad \mathbf{K}_1 := \begin{pmatrix} 0 & 0 & -c_{12} \\ 0 & 0 & -c_{22} \\ c_{12} & c_{22} & 0 \end{pmatrix}, \quad \mathbf{K}_0 := \begin{pmatrix} 0 & 0 & 0 \\ 0 & 0 & 0 \\ 0 & 0 & -c_{22} \end{pmatrix}, \end{gathered} \tag{10}$$

and $\mathbf{K}_i$ $(i = 0, 1, 2)$ are stiffness matrices, $\mathbf{u}$, $\mathbf{p}$ displacement and load vectors, respectively.

3 Identification of the elastic coefficients

3.1 Identification algorithm

The identification of the constitutive matrix is carried out following the homogenization procedure outlined in [32,35] for a grid beam. This approach enforces an appropriate energy equivalence between the (fine) 3D model and the (coarse) 1D Timoshenko beam, as detailed below. Consequently, the identification developed here seeks to extend the mixed homogenization approach to the granular microstructure under consideration.

The first stage of the identification algorithm calls for establishing a discrete mapping that connects the displacements of the fine model (remember Fig. 2a) with those of the coarse model (remember Fig. 2b). Since the grain beam's structure is non-homogeneous, identification is carried out at selected sampled abscissas, namely $x_i := i\,h$ $(i = 0, 1, ..., n)$, where h represents the already defined period of the microstructure (Fig. 1). At each x_i, the fine model possesses a cross-section $\mathcal{D}_i$ occupying a domain of the (y, z)-plane, which coincides with the external semi-grain's edge; two successive cross-sections $\mathcal{D}_i$, $\mathcal{D}_{i+1}$ bound a cell. To define a discrete map, a kinematic constraint is imposed: the sampled cross-section $\mathcal{D}_i$ is assumed to remain plane, while displacements within the cells are left unconstrained. The rigid displacement of $\mathcal{D}_i$ can be written as:

$$\begin{pmatrix} \tilde{u}\,(x_i, y) \\ \tilde{v}\,(x_i, y) \end{pmatrix} = \begin{pmatrix} u\,(x_i) \\ v\,(x_i) \end{pmatrix} + \begin{bmatrix} 0 & -\theta\,(x_i) \\ \theta\,(x_i) & 0 \end{bmatrix} \begin{pmatrix} x_i \\ y \end{pmatrix}, \quad \text{in}\,\mathcal{D}_i, \quad i = 0, 1, \ldots, n, \tag{11}$$

in which, throughout the paper, the tilde denotes a quantity relevant to the fine model. It is important to emphasize that the rotation of the (flexurally) rigid cross-section of the equivalent Timoshenko beam model should be understood as the averaged rotation of the (flexurally deformable, i.e. warpable) sampled cross-section of the grain beam.

The second stage of the identification algorithm involves the so-called 'cell analysis', which requires enforcing the equivalence of elastic energies stored in a 3D cell and a 1D beam segment of equal length, when both models experience identical displacements at their ends.

In particular, in this stage the averaged energy density of the 3D cell, namely $\tilde{\phi} := \tilde{U}/h$, $\tilde{U}$ being the elastic energy of the 3D cell, is determined as a function of the configuration variables of the 1D beam, according to Eq. (11), as:

$$\tilde{\phi} = \frac{1}{h}\tilde{U}\left(u\,(x_i)\,, v\,(x_i)\,, \theta\,(x_i)\,, u\,(x_{i+1})\,, v\,(x_{i+1})\,, \theta\,(x_{i+1})\right). \tag{12}$$

Finally, the last step of the procedure entails the comparison between the energy densities ϕ and $\tilde{\phi}$, in Eqs. (4) and (12), respectively. This is accomplished by expressing the displacements in terms of strains. Accordingly, the strain–displacement relationships Eq. (1) are integrated in the $(x_i,\ x_{i+1})$-interval, given a suitable strain test field. By taking the (simplest) constant strain field, the end displacements read (rigid motions removed):

$$\begin{aligned} u\,(x_i) &= 0, & u\,(x_{i+1}) &= \varepsilon\,h, \\ v\,(x_i) &= 0, & v\,(x_{i+1}) &= \gamma\,h + \frac{1}{2}\kappa\,h^2, \\ \theta\,(x_i) &= 0, & \theta\,(x_{i+1}) &= \kappa\,h. \end{aligned} \tag{13}$$

Substituting Eq. (13) in Eq. (12), and by enforcing the equality:

$$\phi = \tilde{\phi}, \qquad \forall\,(\varepsilon, \gamma, \kappa)\,, \tag{14}$$

the elastic constants $\mathbf{C} := \left(c_{ij}\right)$ are found.

It is worth noting that the cell's boundary displacements, as defined in Eq. (13), can be interpreted as the superposition of three independent deformation modes, specifically:

- an extensional mode (E), in which $\mathcal{D}_{i+1}$ translates along x-direction;
- a shear mode (S), in which $\mathcal{D}_{i+1}$ translates along y-direction;
- a flexural mode (F), in which $\mathcal{D}_{i+1}$ rotates around the z-axis, respectively, and translates transversely along the y-direction.

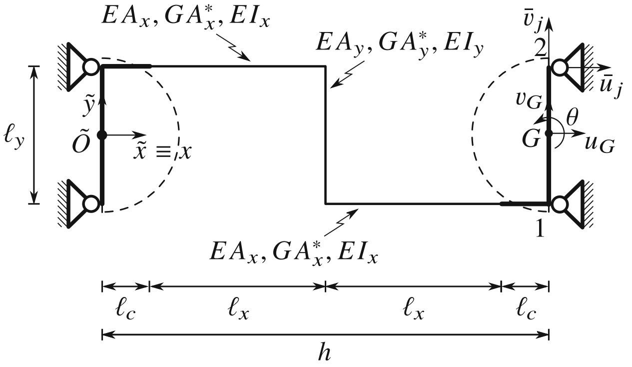

Fig. 3 Periodic microstructure of the grain beam modeled as an assembly of Timoshenko beams, rigidly connected to the grain-pairs

Finally, it is worth highlighting that, under certain simplifying assumptions about the cell's microstructure, the closed-form expression of the cell's elastic energy can be derived analytically. This result, often the most challenging step in the identification process, is achievable in the present case due to the simple fiber arrangement, i.e. when modeled as beams, and the assumption of rigid boundary cross-sections, which neglect micro-warping and account for the contribution of the (rigid) half-grains. However, in cases where the interconnecting elements cannot be modeled as beams or the grains cannot be treated as rigid bodies, a numerical identification procedure, such as one based on FE analysis, becomes mandatory, as will be discussed shortly.

3.2 Analytical identification

The procedure for the analytical evaluation of $\tilde{\phi}$ is detailed as follows. First, some modeling assumptions concerning the microstructure in Fig. 1 are introduced. It is considered as made of rigid-body semi-grains, interconnected to each other through sufficiently slender bodies, i.e. the fibers, which, in turn, are assumed to behave as Timoshenko (micro) beams, of length ℓ_x and ℓ_y, and rectangular cross-sections of sides t_z and t_ν $(\nu = x, y)$, whose assembly results in a planar frame. Another modeling assumptions is relevant to the choice of the length ℓ_c, since it quantifies the extension of the region in which a transition between a rigid-body behavior, i.e. that of the semi-grains (whose boundaries are denoted in red in the figure), and a deformable one, i.e. that of the fibers, occurs. These regions, assumed to behave as rigid-bodies, are shaded in gray in Fig. 1, from which it is also apparent that the definition of the length ℓ_c is not unique, i.e. it can be chosen in a range which varies (approximatively) from zero, for extremely thin horizontal beams, when compared to the radius of the grain and, as denoted in figure, up to the distance between the vertical diameter and the intrados or extrados of the horizontal beams. It is worth noting that the choice made here appears to be the most appropriate for describing the effective (i.e., deformable) length of the horizontal fibers, particularly when they are sufficiently slender and assumed to behave as Timoshenko beams connected to rigid grains.

Each fiber constituting the frame is characterized by axial, shear, and bending stiffnesses, namely EA_ν, GA_ν^*, and EI_ν t_ν, E and G being the elastic and tangential modulus, respectively, $A_\nu = t_\nu \times t_z$ the fiber's cross-section area, $A_\nu^* = 5/6\,(t_\nu \times t_z)$ the shear area, $I_\nu = 1/12\left(t_\nu^3 t_z\right)$ the inertia moment with respect to its cross-section principal axis, parallel to $z-$axis, respectively $(\nu = x, y)$. With these assumptions, the fine model of the granular microstructure is schematized as reported in Fig. 3, where the axis-line of three Timoshenko beams is sketched; this assembly is rigidly connected at its ends to the grain's centroids (ideally) through rigid bars (denoted with a thicker line in the figure). The rigid bars located at the cross-sections $\mathcal{D}_i$ and $\mathcal{D}_{i+1}$, which represent the grain and therefore delimit the cell, are restrained at the cell's periodicity joints by external hinges.

Once the cell is modeled, its elastic energy is evaluated by assigning the above-mentioned deformation modes, i.e. by applying proper boundary displacements at the (periodicity) hinges (denoted with 1 and 2 in Fig. 3), and by pursuing a static analysis of the planar frame. In particular, the (left) cross-section $\mathcal{D}_i$ is kept fixed and a suitable rigid motion is assigned to the (right) cross-section $\mathcal{D}_{i+1}$, according to Eq. (13). More precisely, as already mentioned, this can be interpreted as the superposition of three pure deformation modes: extensional (E), shear (S), and flexural (F). Furthermore, since there are three strains, corresponding to the three independent deformation modes of the cell, and six unknown elastic constants, all the possible combinations of

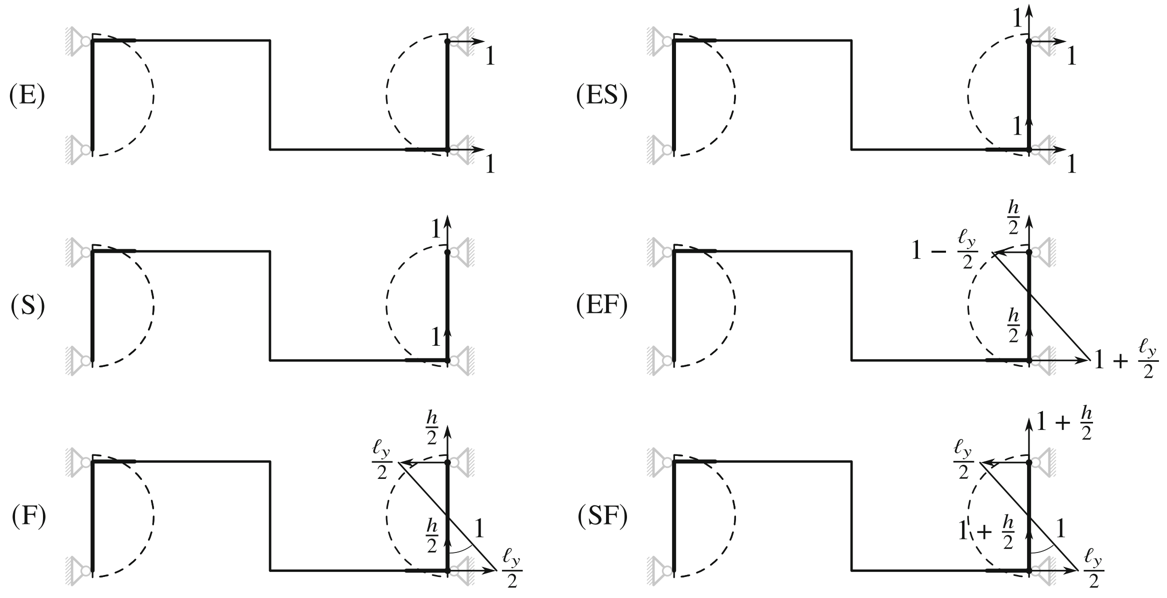

Fig. 4 Deformation modes assigned to the periodic microstructure modeled as an assembly of Timoshenko (micro) beams: (E) extensional; (S) shear; (F) flexural; (ES) extensional and shear; (EF) extensional and flexural; (SF) shear and flexural

the independent modes must be systematically selected and applied to the cell. In this way, coupled deformation modes, identified through the superposition of effects, are also applied to the cell, namely: extensional and shear (ES), extensional and flexural (EF), and shear and flexural (SF). Of course, when a coupled mode is applied, the energy of the involved deformation modes needs to be subtracted from the energy of the coupled ones.

In particular, this procedure can be pursued starting from Eq. (13), which also defines the displacements of the centroid G of the cross-section $\mathcal{D}_{i+1}$, reads: $u_G = u\,(x_{i+1})$, $v_G = v\,(x_{i+1})$ and $\theta = \theta\,(x_{i+1})$. Then, for each deformation mode to be assigned in the algorithm, i.e. for a known set of centroid displacements, Eq. (11) supplies the (rigid) displacements $\tilde{u}\left(x_{i+1}, \mp\ell_y/2\right) =: \bar{u}_j$, $\tilde{v}\left(x_{i+1}, \mp\ell_y/2\right) =: \bar{v}_j$ of the j−th hinges ($j = 1, 2$), namely (remember that $\tilde{O}$ is different from G):

$$\bar{u}_j = u_G \pm \theta \frac{\ell_y}{2}, \quad \bar{v}_j = v_G + \theta\,(\tilde{x}_{i+1} - h) = v_G, \quad \text{with} \quad j = 1, 2. \tag{15}$$

However, from a computational point of view, it is more convenient to: (i) assign unitary displacements at the hinges, (ii) express the centroid displacements by using Eq. (15), and (iii) evaluate the associated strains through Eq. (13). By summarizing, the algorithm to apply is detailed in what as follows.

1. Extensional mode (E) is assigned, in which $\mathcal{D}_{i+1}$ translates axially. Therefore, $\bar{u}_j = 1$ ($j = 1, 2$) is set and, since $u_G = 1$, $v_G = 0$, $\theta = 0$, then $\varepsilon = 1/h$, $\gamma = 0$, $\kappa = 0$; c_{11} is computed.
2. Shear mode (S) is assigned, in which $\mathcal{D}_{i+1}$ translates transversely. Therefore, $\bar{v}_j = 1$ ($j = 1, 2$) is set and, since $u_G = 0$, $v_G = 1$, $\theta = 0$, then $\varepsilon = 0$, $\gamma = 1/h$, $\kappa = 0$; c_{22} is computed.
3. Flexural mode (F) is assigned, in which $\mathcal{D}_{i+1}$ rotates around the z-axis and translates transversely. Therefore, $\bar{u}_j = -\tilde{y}_j$ together with $\bar{v}_j = h/2 + \tilde{x}_j$ ($j = 1, 2$) are set; since $u_G = 0$, $v_G = h/2$, $\theta = 1$, then $\varepsilon = 0$, $\gamma = 0$, $\kappa = 1/h$; c_{33} is computed.
4. Extensional and shear mode (ES), i.e. the superposition of the pure modes (E), (S), is assigned, for which $\varepsilon = 1/h$, $\gamma = 1/h$, $\kappa = 0$; since c_{11}, c_{22} are known, c_{12} is computed.
5. Extensional and flexural mode (EF), i.e. the superposition of the pure modes (E), (F), is assigned, for which $\varepsilon = 1/h$, $\gamma = 0$, $\kappa = 1/h$; since c_{11}, c_{33} are known, c_{13} is computed.
6. Shear and flexural mode (SF), i.e. the superposition of the pure modes (S), (F), is assigned, for which $\varepsilon = 0$, $\gamma = 1/h$, $\kappa = 1/h$; since c_{22}, c_{33} are known, c_{23} is computed.

Remarkably, for each of the (pure and coupled) assigned deformation mode, an analytical (exact) solution of the elasto-static problem for such a planar frame, subject to given displacements at the right hinges, as shown in Fig. 4, is determined; accordingly, displacement, strain and stress fields of the k-th Timoshenko beam, with

$k = 1, 2, 3$ are found. In particular, for each of the six problems shown Fig. 4, the elastic energy of the cell $\tilde{U}$, is evaluated as the sum of the elastic energy of the k-th beam $\tilde{U}_k$, namely:

$$\tilde{U}(\varepsilon, \gamma, \kappa) = \sum_{k=1}^{3} \tilde{U}_k, \quad \text{with} \quad k = 1, 2, 3, \tag{16}$$

where:

$$\begin{aligned} \tilde{U}_k(\varepsilon, \gamma, \kappa) &= \frac{1}{2}\int_0^{\ell_x} \left(EA_x\varepsilon_k^2 + GA_x^*\gamma_k^2 + EI_x\kappa_k^2\right) \mathrm{d}x, \quad \text{with} \quad k = 1, 2, \\ \tilde{U}_3(\varepsilon, \gamma, \kappa) &= \frac{1}{2}\int_0^{\ell_y} \left(EA_y\varepsilon_3^2 + GA_y^*\gamma_3^2 + EI_y\kappa_3^2\right) \mathrm{d}x, \end{aligned} \tag{17}$$

in which $\tilde{U}_1$ and $\tilde{U}_2$ are the elastic energies of the horizontal fibers and $\tilde{U}_3$ is that of the vertical one. Finally, since $\tilde{\phi} = \tilde{U}/h$, the Green's law Eq. (5) supplies for the elastic matrix $\mathbf{C}$. As already mentioned, a shear-axial displacement coupling at the macro-scale is observed in the case at hand, so that Eq. (7) turns out to be defined as:

$$\mathbf{C} = \begin{pmatrix} c_{11} & c_{12} & 0 \\ & c_{22} & 0 \\ \text{SYM} & & c_{33} \end{pmatrix}, \tag{18}$$

where the chiral behavior is represented by the fact that $c_{12} \neq 0$. The analytical expression of the elastic coefficients is reported in Appendix A for both the cases $t_x \neq t_y$ and $t_x = t_y$.

3.3 Numerical identification

Following the same steps described for the analytical identification, a numerical identification of the elastic matrix is also pursued in this paper. The procedure is outlined in [33], when a framed microstructure is taken into account and here extended to a grain beam for which the cell is modeled as a 2D Cauchy continuum. Therefore, grains are deformable but, as in the analytical identification, cross-sections $\mathcal{D}_i$ and $\mathcal{D}_{i+1}$ are assumed as rigid-bodies. Moreover, to better understand the effect of the presence of the grains in the model, the numerical identification is developed under two different cases (see Fig. 5), namely with and without grains, named respectively NC (Numerical Cauchy, Fig. 5a) and NC-ng (Numerical Cauchy - no grains, Fig. 5b). Accordingly, in the former model, the grains contribute to the elastic energy of the cell with their deformability, while in the latter no contribution is given since they behave as rigid bodies. Furthermore, in the former case the cross-sections $\mathcal{D}_i$ and $\mathcal{D}_{i+1}$ are hinged at the periodicity joints while in the latter one the cell is considered as clamped in the correspondence of the boundary between the grains and the horizontal fibers.

For each deformation mode, the displacements u_G, v_G and θ of the centroid of the cross-section $\mathcal{D}_{i+1}$ are the same considered in the analytical identification procedure. Also those to be applied at the hinged joints are the same in the NC case (Fig. 5a); while, for the NC-ng case (Fig. 5b), they are evaluated at the clamped boundary through Eq. (15).

The algorithm for the evaluation of the constitutive matrix, in the numerical identification procedure, consists of two steps:

1. in the first step a FE analysis of the cell is performed and its elastic energy evaluated, for each assigned deformation mode, through the application of the Clapeyron's theorem, namely: (i) $\tilde{U} = \frac{1}{2}\sum_{j=1}^{2}\left(r_{xj}\bar{u}_j + r_{yj}\bar{v}_j\right)$, for the NC case in Fig. 5a, where r_{xj} and r_{yj} are the horizontal and vertical components of the hinges' reactions, respectively; (ii) $\tilde{U} = \frac{1}{2}\int_0^{\ell_s}\left[r_x(s)\,\bar{u}(s) + r_y(s)\,\bar{v}(s)\right]\mathrm{d}s$ for the NC-ng case in Fig. 5b, where $r_x(s)$ and $r_y(s)$ are the (distributed) horizontal and vertical components of the clamp reactions in the $[0, \ell_s]$ clamped region, spanned by the s abscissa, expending work on the horizontal and vertical components of the displacement $\bar{u}(s)$ and $\bar{v}(s)$, respectively;
2. then, by requiring Eq. (14) holds for any $\varepsilon, \gamma, \kappa$ in which $\tilde{\phi} = \tilde{U}/h$, the unknown six elastic constants are computed.

Finally, it is worth to notice that the first step of the algorithm calls for assigning proper boundary displacements at the cell, in the same way described in Sect. 3.1, which is graphically recalled for the case of cell modeled as a Cauchy 2D-elements assembly (Fig. 6).

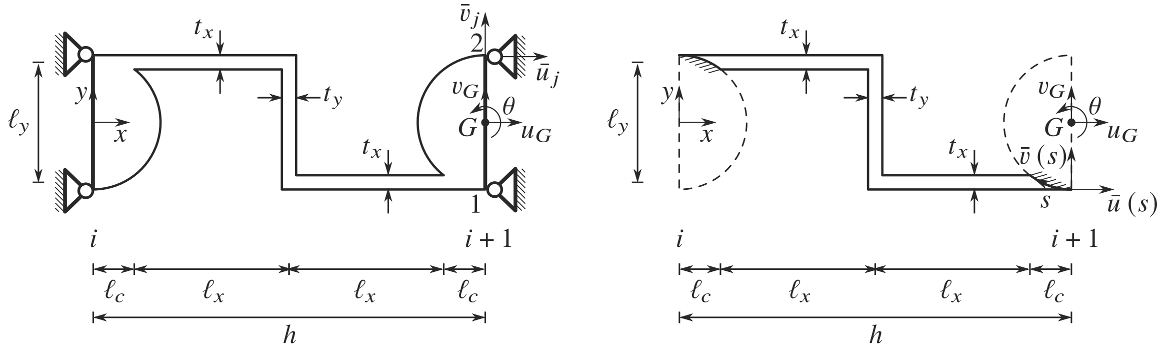

(a) (b)

Fig. 5 Periodic microstructure of the grain beam modeled as an assembly of plate/membrane (2D Cauchy continuum): **a** with grains; **b** without grains

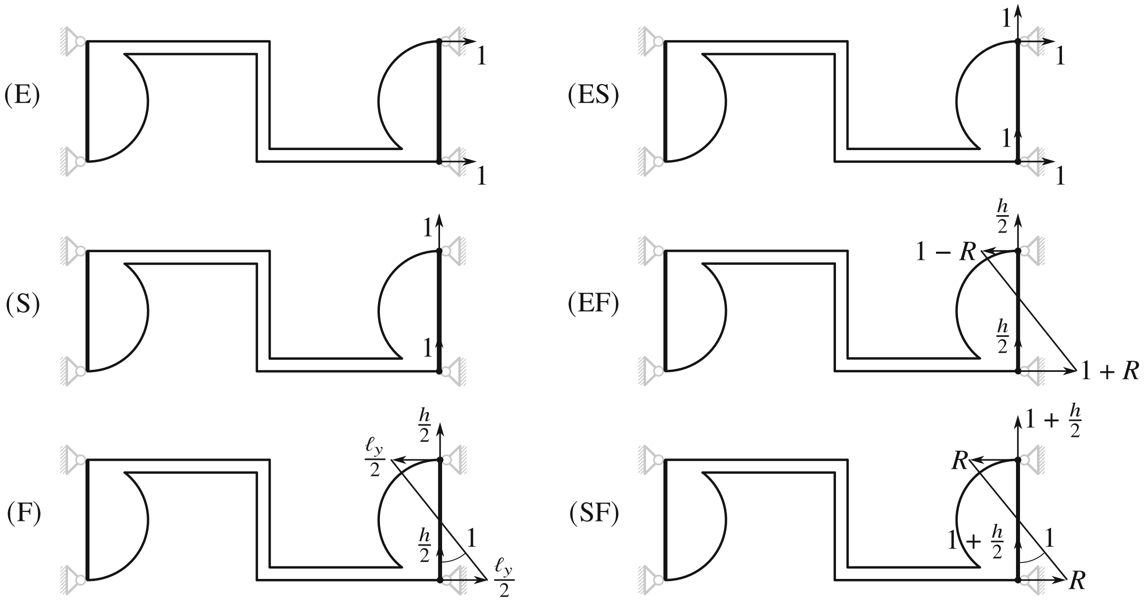

Fig. 6 Deformation modes assigned to the periodic microstructure modeled as a plate assembly (Cauchy 2D): (E) extensional; (S) shear; (F) flexural; (ES) extensional and shear; (EF) extensional and flexural; (SF) shear and flexural

4 Qualitative analysis of the mechanical behavior

The analytical identification of the constitutive matrix supplies closed-form expressions which relates micro and macro quantities, see Eqs. (25) and (27) in Appendix A. Such identification gives the possibility to design the microstructure behavior, aiming at obtaining a targeted macroscopic behavior of the grain beam.

To accomplish this task, in this section a qualitative analysis of the mechanical behavior of the grain beam is carried out by conducting a parametric analysis of the identified constitutive coefficients while varying the geometric characteristics of the microstructure. The analysis is carried out by considering the horizontal and vertical fibers of the same cross-section, i.e. $t_z \times t$, with $t = t_x = t_y$, and, therefore, $A_\nu = A$, $A^*_\nu = A^*$, $I_\nu = I$, the radius of gyration of the cross-section is defined as $\rho = \sqrt{I/A}$, as well as the nondimensional beam's stiffness ratio $\mu_\nu = 12EI/GA^*\ell_\nu^2$ with respect to ν-axis ($\nu = x, y$). Given the geometry of the cell shown in Fig. 1, the following relations hold:

$$h = 2\left(\ell_c + \ell_x\right), \quad \ell_c = \sqrt{t\left(2R - t\right)}, \quad \ell_y = 2R - t. \tag{19}$$

Then, it is useful to introduce two nondimensional parameters, namely $\alpha := h/2R$ and $\beta := \ell_x/\ell_y$, which represent, respectively the aspect ratio of the cell, i.e. the ratio between its length and height, and the ratio between the lengths of horizontal and vertical beams. By making use of Eqs. (19), it is:

$$\beta = \frac{\alpha - \sqrt{\eta\,(2-\eta)}}{2-\eta}, \tag{20}$$

where $\eta := t/R$, is the nondimensional thickness-radius ratio. Equation (20) shows that, for a given cell's aspect ratio α (and radius R), β (nonlinearly) depends on the η and, as it will be clear soon, it can be seen as an (indirect) measure of the fibers' slenderness. In particular, within the range $0 < \eta < 1$, for which $R > t$, from Eqs. (19) and (20), it can be observed that: (i) when $\eta \to 0$, i.e. the fibers have a vanishing thickness ($t \to 0$), then $\beta \to \alpha/2$, $\ell_y \to 2R$, $\ell_c \to 0$, $h \to 2\ell_x$; (ii) when $\eta \to 1$, i.e. the fibers have a thickness comparable to the grain's radius ($t \to R$), then $\beta \to \alpha - 1$, $\ell_y \to R$, $\ell_c \to R$, $h \to 2\,(R + \ell_x)$. Moreover, in the (limit) case $\eta \to 2$, occurring when the fibers have a thickness comparable to the double of the grain's radius ($t \to 2R$), then $\beta \to \infty$, thus entailing that the horizontal fibers are superimposed and the vertical fiber no longer exist, namely $\ell_y \to 0$, together with $\ell_c \to 0$ and $h \to 2\ell_x$.

In order to better highlight the meaning of the parameter β, Eq. (20) is expanded in series for small η (retaining α of order one in the expansion), thus obtaining:

$$\beta \simeq \frac{\alpha}{2} - \frac{\sqrt{\eta}}{\sqrt{2}} + \frac{\alpha\eta}{4} + \mathcal{O}\left(\eta^{3/2}\right). \tag{21}$$

Equation (21) shows that β differs from $\alpha/2$ due to a small (not vanishing) η and it can increase or decrease with η depending on the magnitude of the second and third term on the right side of Eq. (21). Indeed, from Eq. (21) it can be estimated that: when $\eta > \eta_{lim} := 8/\alpha^2$, then β increases with η, i.e. the greater is β the thicker are the fibers; on the contrary, when $\eta < 8/\alpha^2$, then β decreases with η, i.e. the greater is β the slender are the fibers. Furthermore, an exact analysis of the dependency of η from the parameters α and β can be simply pursued. In particular, by squaring and manipulating Eq. (20), an algebraic second-order equation for η is obtained, namely:

$$\left(1+\beta^2\right)\eta^2 + \left(2\alpha\beta - 4\beta^2 - 2\right)\eta + (\alpha - 2\beta)^2 = 0, \tag{22}$$

from which two roots $\eta_{\pm}\,(\alpha, \beta)$ can be found namely:

$$\begin{aligned}
\eta_{+}\,(\alpha,\beta) &= \frac{1-\alpha\beta+2\beta^2+\sqrt{1+2\alpha\beta-\alpha^2}}{1+\beta^2} \quad && \text{if } \alpha > 1 \quad \text{and} \begin{cases} \alpha > 2\beta \text{ and } \alpha^2 < 1+2\beta\alpha \\ \text{or} \\ \alpha < 2\beta \end{cases} \\
& && \text{or} \\
& && \text{if } \alpha < 1 \quad \text{and} \quad \alpha \neq 2\beta \\[2ex]
\eta_{-}\,(\alpha,\beta) &= \frac{1-\alpha\beta+2\beta^2-\sqrt{1+2\alpha\beta-\alpha^2}}{1+\beta^2} \quad && \text{if } \alpha > 2\beta \quad \text{and} \begin{cases} \alpha < 1 \\ \text{or} \\ \alpha > 1 \text{ and } 1+2\beta\alpha > \alpha^2 \end{cases}
\end{aligned} \tag{23}$$

where the existence conditions $\alpha > 0$, $\beta > 0$ and $0 < \eta < 2$ are enforced to ensure the positivity of the geometric parameters and the geometric consistency of the cell. Moreover, it is apparent from Eq. (23), that the two roots $\eta_{\pm}\,(\alpha, \beta)$ exist if the radicand $1 + 2\alpha\beta - \alpha^2 > 0$.

Figure 7 shows the diagrams of the roots $\eta_{\pm}\,(\alpha, \beta)$ as the nondimensional parameters α and β vary. In Fig. 7a the 3D plot of the surface $\eta_{\pm} = \eta_{\pm}\,(\alpha, \beta)$ is depicted; it is shown that, to the multivalued function $\eta_{\pm}\,(\alpha, \beta)$, correspond two branches of the surface, which, in turn, are related to the first and second solution of Eq. (22), namely the upper (η_{+}) and the lower branch (η_{-}), respectively. In Fig. 7b, c two α-isolines of the surface $\eta_{\pm}\,(\beta; \alpha)$ are shown, namely for $\alpha = 1.50$ and $\alpha = 5$, respectively, to assess whether the behavior is qualitatively consistent depending on the aspect ratio. In both cases it is found that as β increases: (i) $\eta_{+} = \eta_{+}\,(\beta; \alpha)$ increases leading, for a given radius of the grain, to the design of thicker cells, i.e. cells in which, due to the increasing of the fibers' thickness, the joints between the fibers becomes increasingly thick until $\eta_{+}\,(\beta; \alpha) \to 2$ is reached at $\beta_{max} \to \infty$, as discussed above; (ii) $\eta_{-}\,(\beta; \alpha)$ decreases until it is

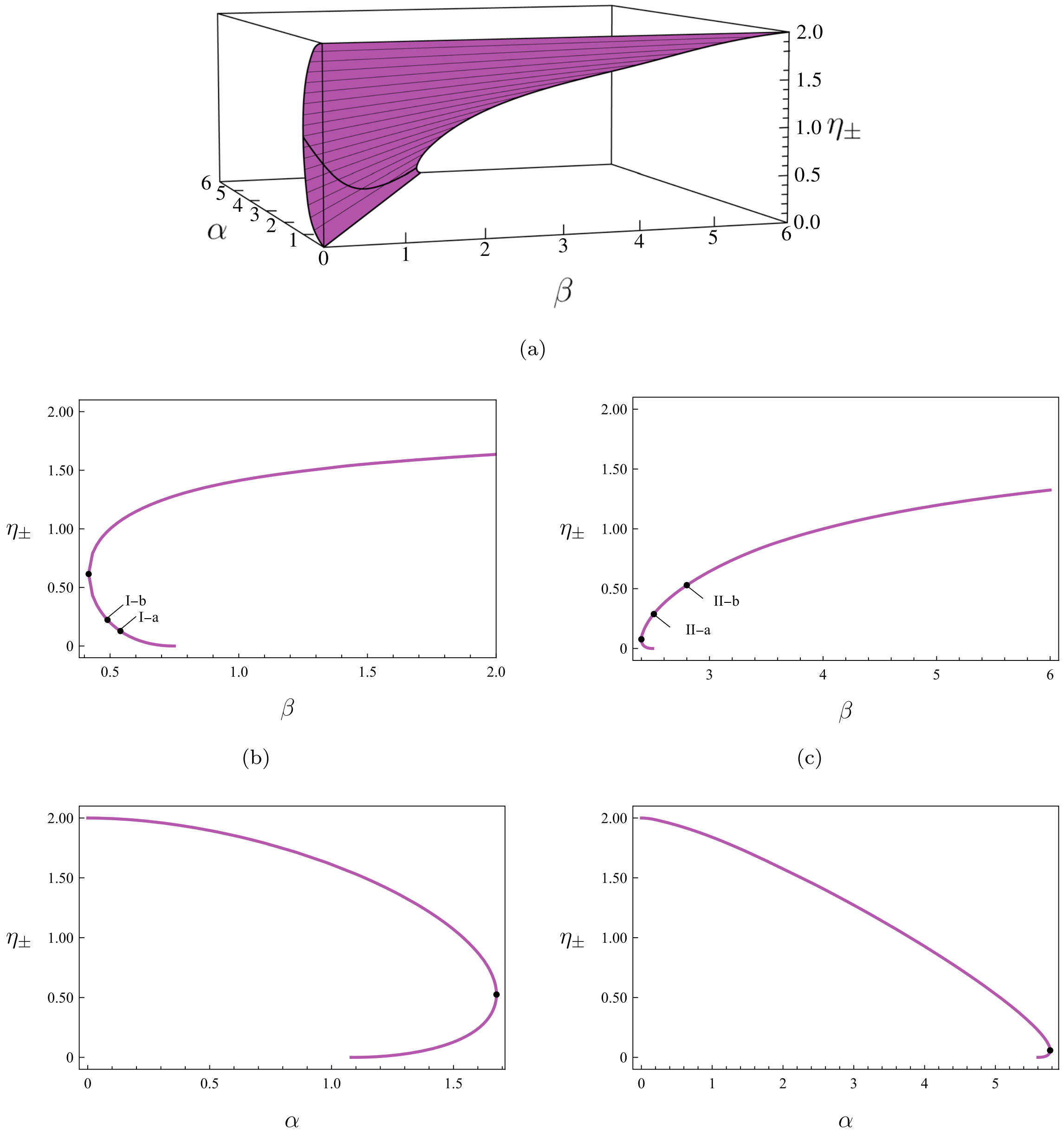

(a)

(b) (c)

(d) (e)

Fig. 7 Plot of the roots $\eta_\pm(\alpha, \beta)$ of Eq. (22): **a** 3D plot $\eta_\pm = \eta_\pm(\alpha, \beta)$; **b**, **c** α-isolines for $\alpha = 1.50$ and $\alpha = 5$, respectively; **d**, **e** β-isolines for $\beta = 0.54$ and $\beta = 2.80$, respectively

equal to zero at $\beta_{max} := \alpha/2$ leading, for a given radius of the grain, to the design of slender cells, i.e. cells composed by an assembly of fibers with thinner sections; (iii) the two branches share the same minimum value $\beta_{min} := \frac{\alpha^2-1}{2\alpha}$, for which $\eta \equiv \eta_{lim} = \frac{2}{1+\alpha^2}$ (highlighted with a black dot in the figure), obtained by setting the radicand in Eq. (23), i.e. the discriminant of Eq. (22), equal to zero, namely: $1 + 2\alpha\beta - \alpha^2 = 0$, and solving for β. Moreover, the trend of $\eta_\pm(\beta; \alpha)$ is qualitatively unchanged in the two cases considered, even if when $\alpha = 5$, the greater aspect ratio allows greater heights of the beam and, therefore, the upper branch is more extended respect to the one obtained for $\alpha = 1.50$.

Analogous considerations can be made when observing the isolines $\eta_\pm(\alpha; \beta)$ for fixed values of β. In Fig. 7d, e two β-isolines of the surface are shown, namely for $\beta = 0.54$ and $\beta = 2.80$, respectively. In both cases it is found that as α decreases: (i) $\eta_+(\alpha; \beta)$ increases until $\eta_+(\alpha; \beta) \to 2$ is reached at $\alpha_{min} := 0$; (ii)

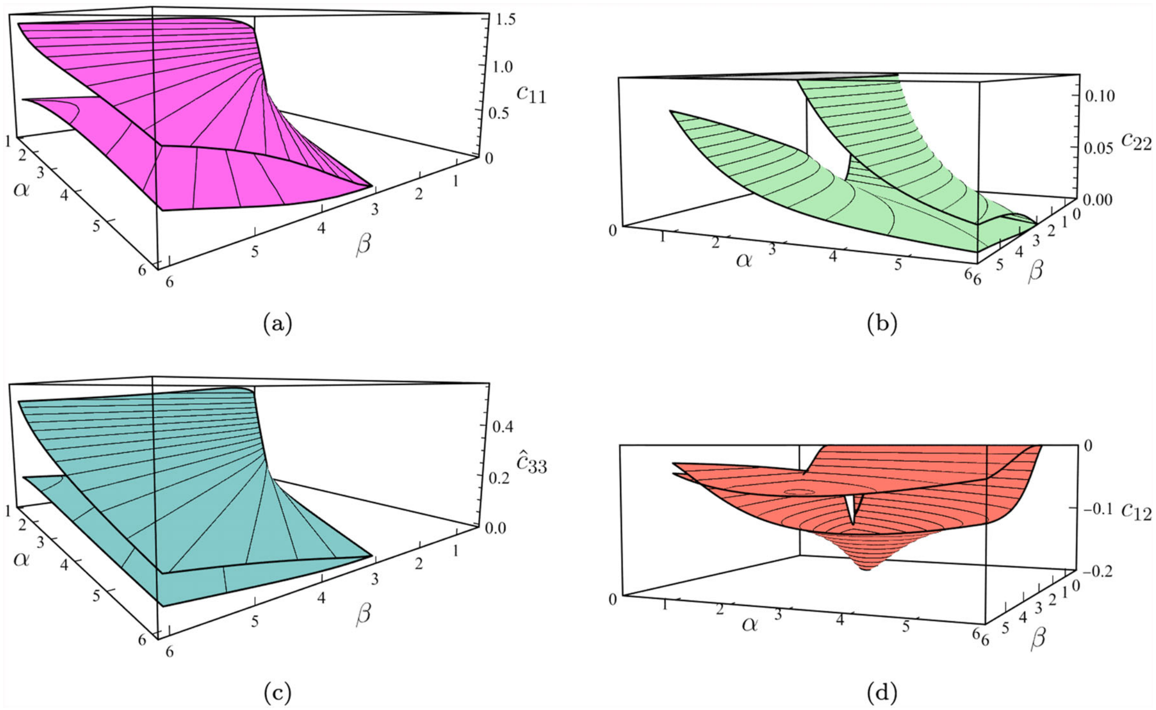

(a) (b)

(c) (d)

Fig. 8 Plot of the elastic coefficients $c_{ij} = c_{ij}(\alpha, \beta)$: **a** $c_{11} = c_{11}(\alpha, \beta)$; **b** $c_{22} = c_{22}(\alpha, \beta)$; **c** $\hat{c}_{33} = \hat{c}_{33}(\alpha, \beta)$; **d** $c_{12} = c_{12}(\alpha, \beta)$

$\eta_-(\alpha; \beta)$ decreases until zero is attained at $\alpha_{min} = 2\beta$; (iii) the two branches share the same maximum value $\alpha_{max} := \beta + \sqrt{1+\beta^2}$, for which $\eta \equiv \eta_{lim} = 1 - \frac{\beta}{\sqrt{1+\beta^2}}$, highlighted with a black dot in the figure, obtained again by setting the radicand in Eq. (23), i.e. the discriminant of Eq. (22), equal to zero and solving for α. Again, the trend of $\eta_\pm(\alpha; \beta)$ is qualitatively unchanged in the two considered cases, even if the greater is β, the greater is the extension of the upper branch.

It is important to remark that, the above discussion about the two roots $\eta_\pm(\alpha, \beta)$, which allows to highlight the dependency of the thickness over radius coefficient η upon the parameters α and β, is very useful to design the cell. Indeed, it serves as a guide for designing the interconnecting fibers between the two semi-grains of the cell, thereby enabling the a priori determination of whether the cell is slender or thicker.

In order to analyze the dependence of the constitutive matrix upon parameters α and β, these are firstly introduced in Eq. (27) of Appendix A, by keeping the simplifications made at the beginning of this section. In this way, for a given grain's radius R and thickness of the fibers t_z, the constitutive matrix Eq. (18) is obtained as function of the parameters, namely $\mathbf{C}_\pm = \mathbf{C}_\pm(\alpha, \beta)$, as:

$$\mathbf{C}_\pm(\alpha, \beta) = \begin{pmatrix} \frac{10\alpha p_\pm^2\left(24\beta p_\pm^2+5p_\pm^2+40\beta^3 q_\pm^2\right)}{(1+\beta^2)^3 p_\pm s_\pm} & -\frac{300\alpha\beta^2 p_\pm^2 q_\pm}{(1+\beta^2)^3 s_\pm} & 0 \\ & \frac{10\alpha p_\pm^2\left(20(1+6\beta)(1\mp r_\pm)+(17+40\beta)r_\pm^2\right)}{(1+\beta^2)s_\pm q_\pm} & 0 \\ \text{SYM} & & R^2\frac{\alpha p_\pm^2}{6(1+2\beta)(1+\beta^2)(\mp q_\pm)} \end{pmatrix}, \quad (24)$$

where $p_\pm(\alpha, \beta)$, $q_\pm(\alpha, \beta)$, $r_\pm(\alpha, \beta)$ and $s_\pm(\alpha, \beta)$, are convenient definitions to compact the writing of the constitutive matrix, provided in Appendix A, and in which the subscripts $(\pm)$ refers to the first (Eq. (23a)) and second solution (Eq. 23b) of Eq. (22), which have been used to express the thickness t in terms of α and β, respectively. Accordingly, it is apparent that also the constitutive matrix $\mathbf{C}$ is splits into two matrices, $\mathbf{C}_+(\alpha, \beta)$ and $\mathbf{C}_-(\alpha, \beta)$, depending on each roots of Eq. (22), respectively.

In Fig. 8 the 3D plot of the elastic coefficients, $c_{ij} = c_{ij}(\alpha, \beta)$ is shown: in it, for the sake of representational convenience, the coefficient $\hat{c}_{33} := \frac{c_{33}}{R^2}$ has been defined, that coincides with the bending coefficient c_{33} for a unitary grain's radius. In particular, as it is expected from the previous analysis, two-branches surfaces are found for each c_{ij}, corresponding to the the variation of the coefficients of the matrices $\mathbf{C}_+$ and $\mathbf{C}_-$ in Eq.

(24) as functions of the parameters α and β, respectively. The plots in Fig. 8 are shown in the following order: $c_{11} = c_{11}(\alpha, \beta)$ in Fig. 8a, $c_{22} = c_{22}(\alpha, \beta)$ in Fig. 8b, $\hat{c}_{33} = \hat{c}_{33}(\alpha, \beta)$ in Fig. 8c and $c_{12} = c_{12}(\alpha, \beta)$ in Fig. 8d. Furthermore, in Fig. 9 the α- and β-isolines of the 3D surfaces, which highlight the trend of the two-branches elastic coefficients for the same fixed values of α and β selected above, i.e. $\alpha = 1.50, 5$ (Fig. 9a, b) and $\beta = 0.54, 2.80$ (Fig. 9c, d), are reported. The transition between one branch to the other (denoted with a dot in the subfigures) occurs at $\beta = \beta_{min}$ for the α-isolines in Fig. 9a, b and for $\alpha = \alpha_{max}$ for the β-isolines in Fig. 9c, d.

In particular, with reference to the isoline for the smaller aspect ratio, namely $\alpha = 1.50$, depicted in Fig. 9a, and in the zoomed region, close to β_{min}, at the top right box in the figure, as β increases from β_{min}, the coefficients of $\mathbf{C}_+$ modifies as follows: (i) the axial stiffness c_{11}, although it is not evident within the considered β-interval, manifests a non-trivial behavior since it increases up to a maximum (at $\beta = 5.25$) and then, decreases very slowly; (ii) also the shear stiffness c_{22} manifests a non-trivial behavior since it increases up to a maximum (at $\beta = 0.65$) and then, decreases rapidly; (iii) the bending stiffnesses $\hat{c}_{33}$ monotonically increase with β; (iv) $\hat{c}_{33} < c_{22}$ in the considered β-interval, but for greater β-values, particularly at $\beta = 8.10$, the trend reverses, namely $\hat{c}_{33} > c_{22}$; (iv) the axial-shear coupling stiffness c_{12} exhibits an opposite behavior with respect to the other elastic coefficients (note that upper and lower solutions are inverted for this coefficient), decreasing up to a minimum (at $\beta = 0.54$) and then increasing; (v) all the coefficients c_{ij} of the matrix $\mathbf{C}_+$ tend to a limit value reached at $\beta \to \infty$, namely $c_{11}^{\infty} = 1$, $c_{22}^{\infty} = 0.22$, $\hat{c}_{33}^{\infty} = 0.33$ and $c_{12}^{\infty} = 0$, in which, in particular, the coupling term tends to zero since, for sufficiently large β values, the vertical beam no longer exists. Moreover, the constitutive coefficients of $\mathbf{C}_-$, for the same α-isoline, shows the following trend as β increases from β_{min}: (i) the coefficients c_{ii} $(i = 1, 2, 3)$ decrease, whereas the coupling term c_{12} increases exhibiting, similarly to the constitutive coefficients of $\mathbf{C}_+$, an opposite behavior to that of the c_{ii} coefficients; (ii) consistently with the behavior of $\eta_-(\alpha; \beta)$ in Fig. 7, all the coefficients c_{ij} of the matrix $\mathbf{C}_-$ tend to zero at $\beta = \beta_{max}$.

Then, by focusing on the isoline associated with the larger aspect ratio, i.e. $\alpha = 5$, shown in Fig. 9b and in the zoomed region, close to β_{min}, at the top right box in the figure, it can observed that, as β increases from β_{min}, a qualitatively similar behavior is observed with respect to the former isoline, albeit with some differences. More specifically: (i) the coefficients c_{11}, $\hat{c}_{33}$ and c_{12} of $\mathbf{C}_+$ manifest a qualitatively similar behavior already recognized for the former isoline while c_{22} does not, since it monotonically increase with β. In particular, the axial stiffness increases up to $\beta = 29.71$ and then decreases, while the axial-shear coupling stiffness decreases up to $\beta = 4.77$ and then increases; (ii) a slower growth with β is recognized for all the c_{ij}, toward c_{ij}^{∞} (i.e. toward their values attained at $\beta \to \infty$, which, in this case, are $c_{11}^{\infty} = 1$, $c_{22}^{\infty} = 0.036$, $\hat{c}_{33}^{\infty} = 0.33$ and $c_{12}^{\infty} = 0$); (iii) the elastic coefficients evaluated with the matrix $\mathbf{C}_-$ tend more rapidly to zero at $\beta = \beta_{max}$.

When reference is made to the isoline for the smaller fibers' lengths ratio, namely $\beta = 0.54$, depicted in Fig. 9c, and in the zoomed region, close to α_{max}, at the top right box in the figure, as α decreases from α_{max}, the coefficients of $\mathbf{C}_+$ behaves as follows: (i) c_{ii} $(i = 1, 2, 3)$ monotonically increase and, in particular, it is $c_{22} > c_{11}$, when $\alpha > 0.91$, while, for smaller values, the trend reverses, namely $c_{22} < c_{11}$; (ii) $\hat{c}_{33} < c_{22}$ in the whole α-region; (iii) c_{12}, as for the α-isoline, exhibits an opposite behavior respect to the elastic coefficients c_{ii} in fact, it manifests a non-trivial behavior decreasing up to a minimum (at $\alpha = 1.59$) and then increasing; (iv) for $\alpha \to 0$, all the c_{ii} $(i = 1, 2, 3)$ coefficients of the matrix $\mathbf{C}_+$ tend to infinity, namely $c_{11}^{0} \to \infty$, $c_{22}^{0} \to \infty$, $\hat{c}_{33}^{0} \to \infty$, while the coupling term tends to zero, $c_{12}^{0} \to 0$, since, as mentioned for the previous cases, for small α values the vertical beam, and accordingly the particular geometry that entails the coupling, no longer exists. Moreover, the constitutive coefficients of $\mathbf{C}_-$, for the same β-isoline, shows the following trend, as α decreases from α_{max}: (i) the coefficients c_{ij} exhibit an analogous behavior to that of the constitutive coefficients of $\mathbf{C}_-$ for the α-isoline, i.e. the coefficients c_{ii} $(i = 1, 2, 3)$ decrease, while c_{12} increases; (ii) consistently with the behavior of $\eta_-(\alpha; \beta)$ in Fig. 7, all the coefficients c_{ij} of the matrix $\mathbf{C}_-$ tend to zero at $\alpha = \alpha_{min}$.

Finally, by focusing on the isoline associated with the fibers' lengths ratio, i.e. $\beta = 2.80$, shown in Fig. 9d and in the zoomed region, close to α_{max}, at the top right box in the figure, it can observed that, as α decreases from α_{max}, a qualitatively similar behavior is observed with respect to the former isoline, notwithstanding some differences arise. In particular: (i) the coefficients c_{ij} of $\mathbf{C}_+$ manifest a qualitatively similar behavior already recognized for the former isoline, with the axial-shear coupling stiffness that decreases up to $\alpha = 2.84$ and then increases, but $c_{22} < c_{11}$ in the whole α-region and, moreover, it is $c_{22} < \hat{c}_{33}$ when $\alpha > 2.62$ while, for smaller values, the trend reverses, namely $c_{22} > \hat{c}_{33}$; (ii) a slower growth with α decreasing is recognized

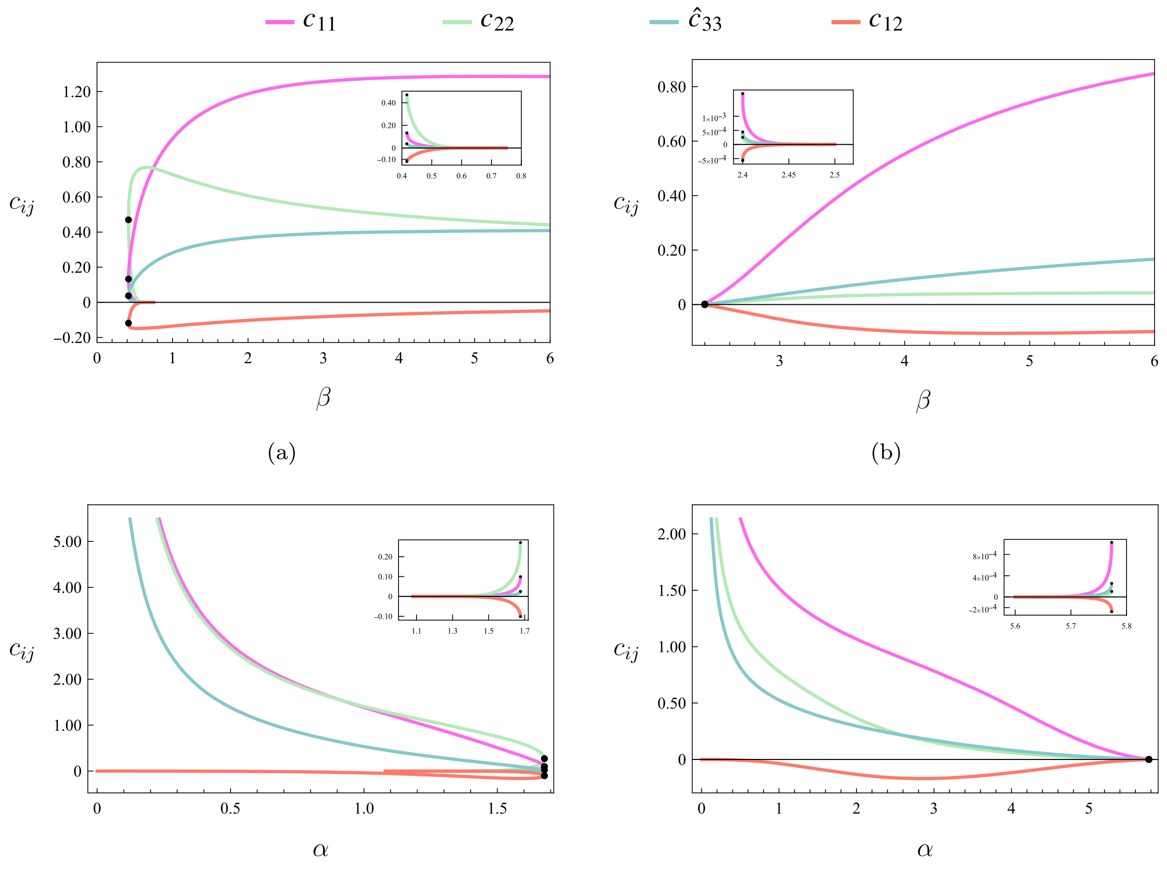

(a) (b)

(c) (d)

Fig. 9 Isolines of the surfaces $c_{ij} = c_{ij}(\alpha, \beta)$ shown in Fig. 8: **a**, **b** α-isolines for $\alpha = 1.50$ and $\alpha = 5$, respectively; **c**, **d** β-isolines for $\beta = 0.54$ and $\beta = 2.80$, respectively

for all the c_{ij}, toward c^0_{ij} (i.e. toward their values attained at 0, which are $c^0_{11} \to \infty$, $c^0_{22} \to \infty$, $\hat{c}^0_{33} \to \infty$ and $c^0_{12} \to 0$); (iii) the elastic coefficients evaluated with the matrix $\mathbf{C}_-$ tends more rapidly to zero at $\alpha = \alpha_{min}$.

In conclusion of this section, it is worth emphasizing that, through the analytical identification of the constitutive matrix and the subsequent parametric analysis conducted here, it becomes possible to design the cell to achieve a targeted set of elastic constants and their associated ratios. In this context, both the macroscopic behavior of the homogenized equivalent beam and its chiral characteristics can be purposefully engineered.

5 Numerical results

Numerical results are referred to four grain beams, taken as case studies, made of Acrilonitrile Butadiene Stirene (ABS), a thermoplastic polymer characterized by an elastic modulus $E = 2180\text{N/mm}^2$, Poisson coefficient $\nu = 0$ and mass density $\rho = 1040\text{kg/m}^3$, taken as case studies. The layout of the bodies that make up the cell is shown in Fig. 1. The geometric dimensions of the case study are defined thanks to the qualitative analysis of mechanical behavior illustrated in Sect. 4.

5.1 Definition of the case studies

Case studies are defined by choosing dimensions R, t_z and parameters α, β. Then, since $\eta_\pm(\alpha, \beta)$, the thickness of the fibers t is determined. Case studies are referred to two value of $\alpha = 1.50$ and $\alpha = 5$ (Fig. 9), and labelled as I and II, respectively; moreover, for each of them two values of β are chosen in such a way the fibers

Table 1 Cell's geometric dimensions

		I-a	I-b	II-a	II-b
ℓ_x	[mm]	5.06	4.35	21.49	20.59
ℓ_y	[mm]	9.36	8.89	8.56	7.35
ℓ_c	[mm]	2.44	3.15	3.51	4.41
t	[mm]	0.64	1.11	1.44	2.65
h	[mm]	15	15	50	50
ℓ	[mm]	330	330	1100	1100

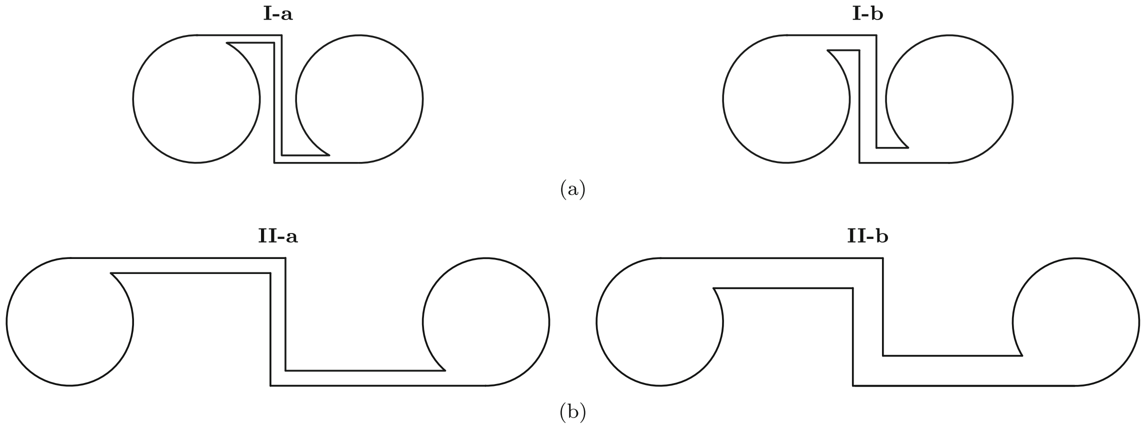

Fig. 10 Case study: **a** I; **b** II

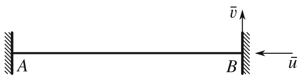

Fig. 11 Analyzed static problem

can be considered, respectively, as: (i) thin fibers, and the relevant case study is denoted with label "-a" and here referred to as "thin cell"; (ii) thick fibers and the relevant case study is denoted with label "-b" and here referred to as "thick cell". Accordingly, in the former case the fibers connecting the grains are sufficiently slender elements, whose behavior can be described by Timoshenko beam's theory, while, in the latter case, they are more similar to plates.

In Fig. 7 are reported the plots of $\eta_\pm\,(\beta;\alpha)$ for the aspect ratios $\alpha = 1.50, 5$. For these cases, the lower branches exist within the ranges $0.416 < \beta < 0.75$ and $2.40 < \beta < 2.50$, respectively. Conversely, the upper branches share the same minimum value of the lower ones ($\beta = 0.416$ and $\beta = 2.40$) and then increase monotonically, approaching the asymptotic limit $\eta_+\,(\beta;\alpha) \to 2$ as $\beta \to \infty$. For case study I, the values of $\eta_\pm$ are chosen from on the α-isoline $\alpha = 1.5$, in the correspondence of lower branch; they are marked with a dot in Fig. 7a. Furthermore, for the case study II, the values of $\eta_\pm$ are selected on the α-isoline $\alpha = 5$, in the correspondence of the upper branch; they are marked with a dot in Fig. 7b. Finally, the chosen values of β are: (i) $\beta = 0.54$ and $\beta = 0.49$, denoted as case study I-a and I-b in Fig. 7a, (ii) $\beta = 2.51$ and $\beta = 2.80$, denoted as case study II-a and II-b in Fig. 7b.

Once α and β are set, all the geometric dimensions of the cell, namely ℓ_x, ℓ_y, ℓ_c and h, are defined using Eqs (19). These are reported in Table 1 and giving rise to the four cells sketched in Fig. 10, where $R = 5$ mm and $t_z = 4$ mm have been chosen.

A doubly-clamped beam at the ends A and B, whose microstructure is made by $n = 22$ cells, is considered for the numerical analyses. No static loads are applied to the beam, i.e. $p_x = p_y = c = 0$, while boundary displacement at the end B are assigned, as represented in Fig. 11, namely: $\bar{u}_B = -1$ mm, $\bar{v}_B = 1$ mm, $\bar{\theta}_B = 0$ mm. The analytical solution for the static problem of the equivalent beam model, under such boundary conditions, is reported in Appendix B (see, Eq. (31)).

Two FE models are build up to validate the homogenized beam model solution and compare numerical (FE) and analytical (exact) solutions, namely: (i) in the first one, here referred to as "Fine Model (Cauchy)", the grain beam is modeled as an assembly of bi-dimensional Cauchy continuum elements, i.e. plate elements; (ii) in the second one, here referred to as "Fine Model (Beams)", the grain beam is schematized as an assembly of Timoshenko beams and rigid bodies. In the former model, the geometry of the grain beam is discretized using a triangular mesh with a quadratic displacement field; in the latter, the geometry is discretized using a fine mesh with a cubic displacement field and a quadratic rotation field. The vertical elements in the Fine Model (Beams) located at $x_i = i\ h$ with $i = 0, 1, \ldots, n$ representing the (rigid) grains and the horizontal elements representing the transition region of length ℓ_c (remember Fig. 3), are accounted for in the model as rigid bodies. Moreover, as an order of magnitude of degrees of freedom for case study I-a, it is approximately $233{\cdot}10^3$ and 870 for Fine Model (Cauchy) and Fine Model (Beams), respectively.

5.2 Discussion about the elastic coefficients

The elastic coefficients for the case studies at hand are obtained through both the analytical (see 3.1) and numerical (see 3.3) identification procedure of the mixed homogenization approach. They are reported in Tables 2 and 3, where NC, NC-ng and AB stand for the constants evaluated with the numerical procedure with grains (Numerical Cauchy), numerical procedure without grains (Numerical Cauchy - no grains) and the analytical procedure (Analytical Beams), respectively. The percentage differences of the elastic constants evaluated with different identification procedures, namely ϵ_1, ϵ_2 and ϵ_3, are reported in the last three columns of each subtable of Table 2 and 3. In particular, naming c_{ij}, c_{ij}^{ng} and c_{ij}^{a} the constitutive coefficients determined with NC, NC-ng and AB, respectively, it is $\epsilon_1 := 100\left(c_{ij} - c_{ij}^{ng}\right)/c_{ij}$, $\epsilon_2 := 100\left(c_{ij}^{ng} - c_{ij}^{a}\right)/c_{ij}^{ng}$ and $\epsilon_3 := 100\left(c_{ij} - c_{ij}^{a}\right)/c_{ij}$.

At first, results obtained from NC and NC-ng cells' homogenization are discussed, related to the percentage difference ϵ_1. It is found that for all the case studies, the constitutive coefficients of NC-ng are always greater than the one evaluated with NC. This is a quite expected result, as it is due to the different modeling of the grain which is deformable in one case (NC) and considered rigid in the other (NC-ng). Therefore, regarding the influence of the grain on the constitutive matrix, it is concluded that, when grain deformability is introduced in the cell schematization, it induces a softening effect on the elastic coefficients.

Afterward, results obtained from the numerical and analytical homogenization procedures are analyzed. First, constitutive coefficients relevant to NC-ng and AB models, related to percentage difference ϵ_2, are considered. In both the cases the grain is considered as a rigid body, and, as it is expected, the percentage differences are quite low for the thinner cells (cases I-a and II-a), with the greater difference being around 6%, while there is a slight increase for the thicker ones (cases I-b and II-b) up about to 11%. These percentage differences are conjectured to be due to two geometric reasons: (i) the modeling choice of the length ℓ_c which, determines the transition region between rigid and deformable behavior at grain-fiber intersection, and (ii) the intersection (joint) between horizontal and vertical fibers which, for the thicker cells, possesses a finite dimension, i.e., nonzero dimension, as opposed to the beam model approximation. More precisely, the slender the beams, the thinner the intersections, the more the joint can be assimilated to the (dimensionless) intersection between beams. It can be concluded that, for thinner cells, the first geometric reason is prevalent in the percentage difference ϵ_2, while, in the thicker ones, both the geometric reasons contribute in the difference ϵ_2.

Finally, results obtained from NC and AB cells' homogenization are discussed, related to the percentage difference ϵ_3. This is the greater difference recognized for the different identification procedures, occurring for all the case studies considered. The higher difference are due to the presence of a deformable grain in the NC model, as well as to the two above-mentioned geometric reasons. However, analytical identification remains sufficiently close to the NC one in the cases of thin cells, while, the percentage differences are greater for the thicker ones. In what follows, the effect of these more pronounced differences will be discussed on the static response of the beam.

5.3 Analysis of the displacement field

The static analysis of the grain beam, which leads to a comparison between the FE model (Beams), the FE model (Cauchy) and the Equivalent beam model, is now discussed. For the latter model, the elastic constants evaluated with the analytical procedure (AB constants) are considered. The comparison is made in terms of longitudinal

Table 2 Elastic coefficients of the equivalent beam model for case studies I-a, I-b and different identification procedures

		NC	NC-ng	AB	ϵ_1	ϵ_2	ϵ_3
I-a							
c_{11}	[N]	23.15	23.58	22.33	−1.84	5.30	3.56
c_{22}	[N]	63.76	69.80	74.46	−9.47	−6.67	−16.77
c_{33}	$\left[\mathrm{N} \times \mathrm{mm}^2\right]$	142.59	145.06	145.68	−1.73	−0.42	−2.16
c_{12}	[N]	−29.51	−31.08	−30.61	−5.34	1.54	−3.72
I-b							
c_{11}	[N]	146.41	152.62	135.07	−4.24	11.50	7.74
c_{22}	[N]	405.60	490.62	542.71	−20.96	−10.62	−33.80
c_{33}	$\left[\mathrm{N} \times \mathrm{mm}^2\right]$	819.09	848.85	855.15	−3.63	−0.74	−4.40
c_{12}	[N]	−185.61	−207.59	−195.80	−11.84	5.68	−5.48

Table 3 Elastic coefficients of the equivalent beam model for case studies II-a, II-b and different identification procedures

		NC	NC-ng	AB	ϵ_1	ϵ_2	ϵ_3
II-a							
c_{11}	[N]	427	435.66	412.20	−2.03	5.39	3.47
c_{22}	[N]	49.35	52.38	52.86	−6.14	−0.89	−7.09
c_{33}	$\left[\mathrm{N} \times \mathrm{mm}^2\right]$	2059.7	2093.3	2094.51	−1.63	−0.06	−1.69
c_{12}	[N]	−122	−127.02	−122.81	−4.11	3.32	−0.66
II-b							
c_{11}	[N]	3414	3600.90	3193.58	−5.47	11.31	6.46
c_{22}	[N]	296.51	338.59	338.94	−14.19	−0.10	−14.31
c_{33}	$\left[\mathrm{N} \times \mathrm{mm}^2\right]$	13430	13908	13886.40	−3.56	0.16	−3.40
c_{12}	[N]	−834.10	−918.14	−846.40	−10.08	7.81	−1.47

displacement $u(x)$, transversal displacement $v(x)$, and rotation $\theta(x)$. In the following plots, the displacement and abscissa unit is mm, while the rotation unit is mrad. The analysis aims to check the effectiveness of the Timoshenko equivalent beam model, grounded on analytical identification of the constitutive coefficients, in reproducing the static behavior of the grain beam.

For case studies I-a and I-b, a very good agreement between the Equivalent beam model (AB constants) and FE model (Beams) is shown in Fig. 12. There is a slight deviation between the FE model (Beams) and FE model (Cauchy), which is more evident for case study I-b. This is due to the modeling of the horizontal fibers as beams that, as discussed above, for the case study I-b, is a strong approximation. The percentage difference, in terms of displacements, between the Equivalent beam model and the discrete FE Model (Cauchy), at the abscissa in which minimum and maximum vertical displacement $v(x)$ is achieved, i.e. at $x = h, 21h$ respectively, is -22% and less than -1% for case study I-a, -49% and less than -1% for case study I-b. The percentage error for the rotation $\theta(x)$ evaluated at the mid-span $x = 11h$ is about -4% and -8% for case study I-a and I-b, respectively. The very good agreement between the Equivalent beam model and FE models is also shown in Fig. 13 where the deformed shape of the grain beam in the case study I-a, is reported. It is important to remark that, the percentage difference determined for $v(h)$ appears to be quite high, even if it is practically not noticeable in Fig. 12; this is due to the fact that the difference arises in the presence of very small vertical displacements (of the order of -0.01mm) rendering the effect negligible. Therefore, a good agreement between the FE model (Cauchy) and the Equivalent beam model is confirmed.

However, it should be remarked that, the high percentage difference, even if is due to numerical approximation of the percentage differences, is also related to the modeling choices of the cell, and, in particular, to the choice of the transition length ℓ_c (see, Sect. 3.1). Indeed, it is evident that reducing ℓ_c in the AB model would result in a larger ℓ_x, thereby producing more slender horizontal fibers. This, in turn, brings the analytical elastic coefficients closer to those of the NC model. More specifically, if one defines ℓ_c as the distance between the vertical diameter of the grain and the intersection of the horizontal fiber's axis line with the grain's circumference, it reduces the percentage difference in displacements between the Equivalent Beam model (using AB constants) and the FE model (Cauchy). However, such a choice would result in the AB model becoming further detached from the NC-ng model, as due to an overestimation of the length of the horizontal beams. Indeed, the choice of ℓ_c was carefully made to ensure that the AB model remained as consistent as possible with the

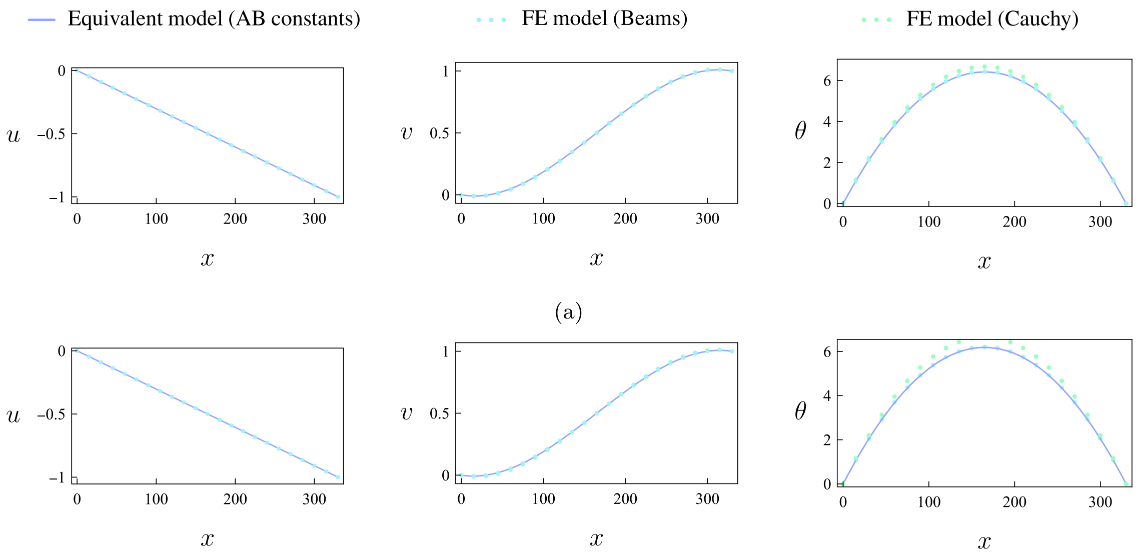

(a)

(b)

Fig. 12 Static response of the Equivalent beam model (AB constants) vs. the discrete FE models (Beams) and (Cauchy) in terms of longitudinal and transversal displacements and rotation of the cross-section for: **a** case study I-a; **b** case study I-b

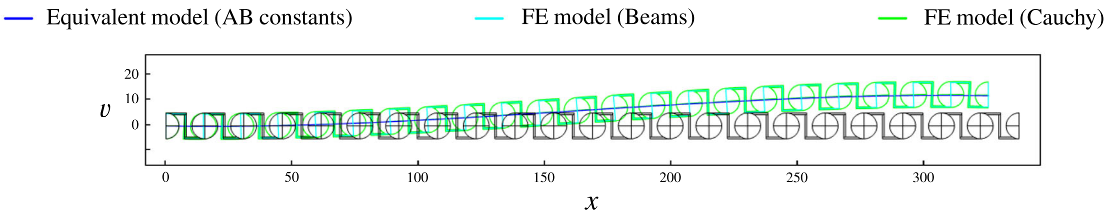

Fig. 13 Comparison between the deformed shapes of the Equivalent beam model (AB constants) and the FE models (Beams) and (Cauchy) for the case study I-a

fine model under the same assumptions, thereby aligning it with the NC-ng model, based on the relevant rigid body assumption for the grains.

It is worth to notice that, the difference between the Equivalent beam model (AB constants) and the FE model (Cauchy), also arises from the choice to use the elastic constants identified with the analytical procedure. In particular, if a more precise solution is desired, the elastic constants evaluated by the NC procedure need to be used (see Fig. 14). In this way, the order of magnitude of the error, in terms of displacements, between Equivalent beam model (with NC constitutive coefficients) and the FE model (Cauchy) at $x = h, 21h$ for the vertical displacement $v(x)$ reveals to be -2% and less than -1% for case study I-a, and -1.5% and less than -1% for case study I-b. The percentage error for the rotation $\theta(x)$ evaluated at $x = 11h$ is less than -1% for both the case studies.

Figure 15 shows the comparison for case studies II-a and II-b, between the static response of Equivalent beam model (AB constants) and FE models (Beams and Cauchy). Results are qualitatively the same as the ones already discussed for cases I-a and I-b, confirming the very good agreement in terms of displacement field which can be obtained with the Equivalent beam model. The percentage difference between the coarse model and the discrete FE Model (Cauchy) evaluated at the abscissa which minimum and maximum vertical displacement $v(x)$ are achieved, i.e. in $x = 3h, 19h$ respectively, is -10% and -2% for case study II-a, -18% and -3% for case study II-b. The percentage error for the rotation $\theta(x)$ evaluated at mid-span $x = 11h$ is about -5% and -10% for case study II-a and II-b, respectively. As in the previous cases, when NC constitutive coefficients are adopted in the Equivalent beam model, the percentage error in terms of vertical displacement $v(x)$, in $x = 3h, 19h$, and rotation $\theta(x)$, in $x = 11h$, between the coarse model and the discrete FE Model (Cauchy) is significantly reduced; in fact the error remains consistently below -2% for both case studies II-a and II-b.

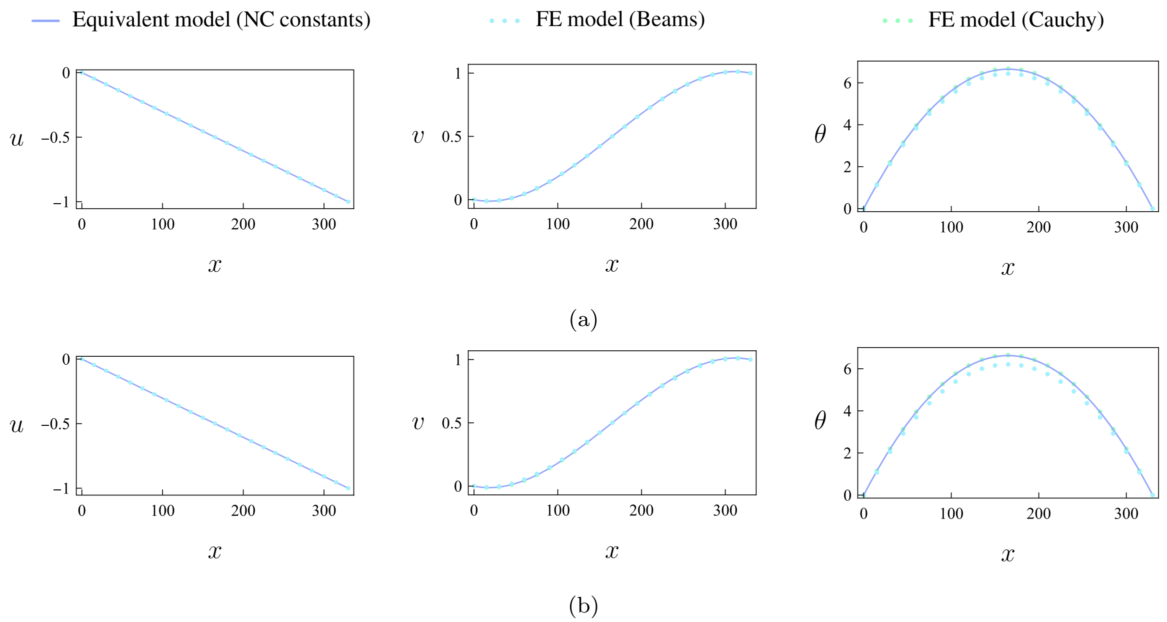

(a)

(b)

Fig. 14 Static response of the Equivalent beam model (NC constants) vs. the discrete FE models (Beams) and (Cauchy) in terms of longitudinal and transversal displacements and rotation of the cross-section for: **a** case study I-a; **b** case study I-b

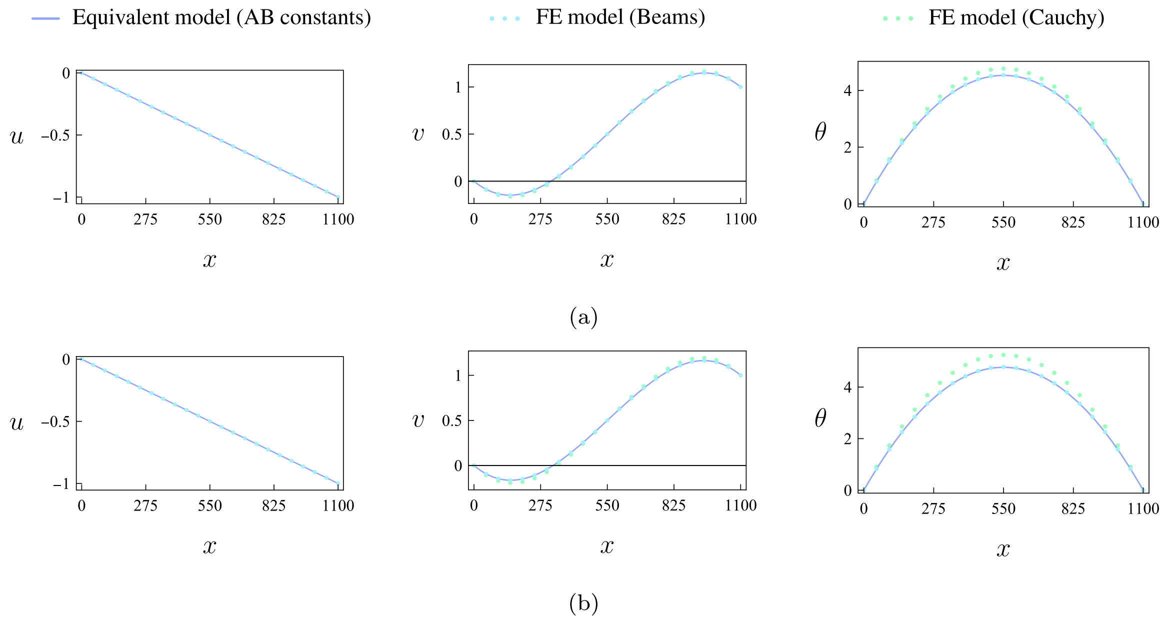

(a)

(b)

Fig. 15 Static response of the Equivalent beam model (AB constants) vs. the discrete FE models (Beams) and (Cauchy) in terms of longitudinal and transversal displacements and rotation of the cross-section for: **a** case study II-a; **b** case study II-b

Finally, to emphasize the chirality, a Timoshenko beam with the diagonal constitutive matrix, is studied. The constitutive matrix is evaluated by considering an equivalent cross-section, such as to obtain the same constitutive matrix used for the grain beam, but without the off-diagonal term.

A clamped beam in A and B, with displacement at the end B and no static loads applied, is considered. Therefore, the same scheme depicted in Fig. 11 is studied but, $\bar{u} = 1$ mm, $\bar{v} = 0$ mm and $\bar{\theta} = 0$. The exact solution for the static problem is discussed in Appendix B for the grain beam, i.e. with $c_{12} \neq 0$; in this case, it will be enough to impose $c_{12} = 0$. The numerical solution is obtained from the FE model (Beams), in which the grain beam is modeled as an assembly of Timoshenko beams. In the Fine Model (Beams) the geometry

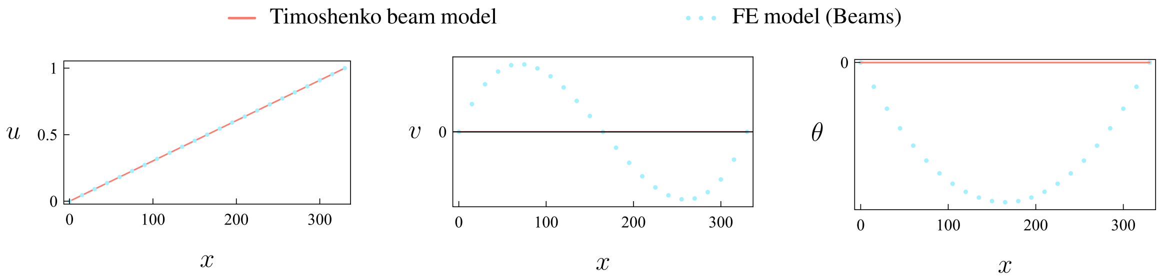

Fig. 16 Static response of the Timoshenko beam model vs. the discrete FE model (Beams) in terms of longitudinal and transversal displacements and rotation of the cross-section for the case study I-a

is again discretized using a fine mesh with a cubic displacement field and a quadratic rotation field. From the comparison between the analytical and numerical solution shown in Fig. 16, the property of chirality is highlighted in fact, when applying a pure extensional mode, the Timoshenko beam model only extends while the grain beam shows the coupling between extensional and shear deformation modes.

6 Conclusions and perspectives

In the present paper, a Timoshenko-like equivalent beam model has been formulated to analyze the static behavior of grain beams. The constitutive law has been determined via a homogenization procedure, based on the energy equivalence between the cell of the periodic grain beam and a segment of the equivalent beam, under the same point-wise displacement fields. The elastic constants have been determined with both analytical and numerical identification procedures and the influence of the deformability of the grain on the constitutive matrix has been detected. A qualitative analysis, grounded on the analytical identification procedure, has been able to reveal the dependence of elastic coefficients upon proper defined nondimensional parameters, as the cell aspect ratio and the slenderness of horizontal and vertical fibers. This is believed to be an important result in terms of designing the microstructure of grain beams in order to achieve a targeted macroscopic response. The chirality of the grain metamaterial has been also highlighted by comparing the analytical and numerical static responses of a grain beam vs that of a classical Timoshenko beam.

The effectiveness and limits of applicability of the Timoshenko-like equivalent beam model have been discussed by numerical analyses, carried out on some grain beams, taken as case studies.

The following conclusions are drawn.

1. The equivalent beam model is effective in describing the static behavior of grain beams.
2. A good agreement between the elastic coefficients obtained through both the analytical and numerical identification procedure is detected, particularly in the cases of thin cells;
3. A good agreement is also detected by comparing the displacement fields obtained by static analysis of the Equivalent beam model (AB) and of the FE models (Beams) and (Cauchy).
4. Numerical identification (NC) of the constitutive matrix of the Equivalent beam Model furnishes an excellent agreement in terms of static response in both the cases of thin and thick cells.

It is important to remark that both the analyzed FE models and the proposed equivalent beam model are based on the assumption of linear kinematics and linear elasticity. A nonlinear analysis could highlight differences related to geometric and constitutive nonlinearities, which are absent in the developed model and would require further investigation.

The main perspective of this work is to validate the obtained results through experimental investigations thanks to Digital Image Correlation (DIC). To this end, uniaxial tests will be performed on samples fabricated with 3D printing technology. Future research will also explore the dynamic behavior of such grain beams. Furthermore, it will be also of interest to analyze the effects of prestress/buckling, as well as the effects of geometric and constitutive nonlinearities and to build up structures through the assembly of chiral objects, so that particular macroscopic behaviors can be achieved.

Author contribution All authors contributed equally to this work. F. D. conceived the scientific idea of this paper and developed analytical solutions. C. P. developed analytical solutions and carried out numerical simulations. The manuscript was written through the contribution of all authors. All authors discussed the results, reviewed and approved the final version of the manuscript.

Funding Open access funding provided by Università degli Studi dell'Aquila within the CRUI-CARE Agreement.

Data availibility No datasets were generated or analysed during the current study.

Declarations

Conflict of interest The authors declare that they have no conflict of interest.

A Analytical expression of the constitutive matrices

The analytical expression of the coefficients of the constitutive matrix in the case $t_x \neq t_y$ is first reported. They reads:

$$
\begin{aligned}
c_{11} &= \frac{12EA_x EI_x EI_y h\left[(4+\mu_x) EA_y \ell_x^3 + 6EI_x \ell_y\right]}{d},\\
c_{22} &= \frac{6EA_y EI_x h\left[\left(1+\mu_y\right) EA_x EI_x \ell_y^3 + 6EA_x EI_y \ell_x \ell_y^2 + 24EI_x EI_y \ell_x\right]}{d},\\
c_{33} &= \frac{EI_x EI_y h}{EI_x \ell_y + 2EI_y \ell_x},\\
c_{12} &= -\frac{36EA_x EA_y EI_x EI_y h \ell_x^2 \ell_y}{d},
\end{aligned}
\tag{25}
$$

where:

$$
\begin{aligned}
d := {} & EA_y \ell_x^3 \left\{EI_x (4+\mu_x)\left[\left(1+\mu_y\right) EA_x \ell_y^3 + 24EI_y \ell_x\right] + 6(1+\mu_x) EA_x EI_y \ell_x \ell_y^2\right\}\\
& + 6EI_x \ell_y \left[\left(1+\mu_y\right) EA_x EI_x \ell_y^3 + 6EA_x EI_y \ell_x \ell_y^2 + 24EI_x EI_y \ell_x\right],
\end{aligned}
\tag{26}
$$

and $\mu_\nu := 12EI_\nu / GA_\nu^* \ell_\nu^2$ $(\nu = x, y)$ is the non-dimensional stiffness ratio.

When $t_x = t_y$, it is $A_x = A_y =: A$, $A_x^* = A_y^* =: A^*$, $I_x = I_y =: I$, and, therefore, $\mu_\nu = 12EI/GA^* \ell_\nu^2$ $(\nu = x, y)$. As a consequence, the constitutive coefficients read:

$$
\begin{aligned}
c_{11} &= \frac{12EA\, EIh\left[(4+\mu_x) EA\ell_x^3 + 6EI\ell_y\right]}{d},\\
c_{22} &= \frac{6EA\, EIh\left[EA\ell_y^2\left(6\ell_x + \mu_y \ell_y + \ell_y\right) + 24EI\ell_x\right]}{d},\\
c_{33} &= \frac{EIh}{2\ell_x + \ell_y},\\
c_{12} &= -\frac{36EA^2 EIh\ell_x^2 \ell_y}{d},
\end{aligned}
\tag{27}
$$

where:

$$\begin{aligned} d := {} & EA^2 \ell_x^3 \ell_y^2 \left[6\ell_x \left(1+\mu_x\right) + \left(4+\mu_x\right)\left(1+\mu_y\right)\ell_y\right] + 144 EI^2 \ell_x \ell_y \\ & + 6EA\,EI \left[4\ell_x^4 \left(4+\mu_x\right) + 6\ell_x \ell_y^3 + \left(1+\mu_y\right)\ell_y^4\right]. \end{aligned} \tag{28}$$

The analytical expression of the constitutive matrix, in terms of the parameter α and β, can be easily found by substituting the geometric relationships listed in Sect. 4. Therefore, by defining:

$$\begin{aligned} p_\pm (\alpha, \beta) &:= \pm\left(1 + 2\beta^2 - \beta\alpha\right) + \sqrt{2\alpha\beta - \alpha^2 + 1}, \\ q_\pm (\alpha, \beta) &:= \pm\left(-1 - \alpha\beta\right) + \sqrt{2\alpha\beta - \alpha^2 + 1}, \\ r_\pm (\alpha, \beta) &:= \frac{p_\pm}{1 + \beta^2}, \\ s_\pm (\alpha, \beta) &:= \mp 1600\beta^3 \left(3\beta + 2\right) + 3200\beta^3 r_\pm \left(3\beta + 2\right) \mp 20 r_\pm^2 \left(440\beta^4 + 336\beta^3 + 144\beta^2 + 54\beta + 5\right) \\ &\quad + 20 r_\pm^3 \left(200\beta^4 + 176\beta^3 + 144\beta^2 + 54\beta + 5\right) \mp r_\pm^4 \left(700\beta^4 + 680\beta^3 + 960\beta^2 + 608\beta + 85\right), \end{aligned} \tag{29}$$

the constitutive matrices of Eq. (24) are obtained.

B Analytical solution of the elastic problem

The analytical (exact) solution for the (elasto-static) boundary value problem (9) is here recalled. When Eq. (9) is specialized for the grain beam, i.e. a beam whose constitutive equation is Eq. (18), in extended form, it reads:

$$\begin{aligned} c_{11} u'' + c_{12}\left(v'' - \theta'\right) + p_x = 0, \\ c_{12} u'' + c_{22}\left(v'' - \theta'\right) + p_y = 0, \\ c_{33}\theta'' + c_{12} u' + c_{22}\left(v' - \theta\right) + c = 0. \end{aligned} \tag{30}$$

The solution of this latter is the sum of the general solution of the homogeneous counterpart of Eq. (30) and the particular solution of the non-homogeneous Eq. (30). The general solution depends on arbitrary constants C_i $(i = 1, \dots, 6)$, determined once the boundary conditions are enforced, namely Eqs. (9)-b and (9)-c. The particular solution is easily evaluated once the loads are specified. In particular, for the case at hand it is $\mathbf{p} = \mathbf{0}$ and $\bar{\mathbf{u}}_B = (\bar{u}, \bar{v}, 0)^T$, so that the solution of the elasto-static problem (30) is found to be:

$$\begin{aligned} u(x) &= \bar{u}\frac{x}{\ell}, \\ v(x) &= \frac{x\left[-c_{12}\,\bar{u}\left(\ell - 2x\right)\left(\ell - x\right) + c_{22}\,\bar{v}\,x\left(3\ell - 2x\right) + 12c_{33}\,\bar{v}\right]}{\ell\left(c_{22}\,\ell^2 + 12c_{33}\right)}, \\ \theta(x) &= \frac{6x\left(\ell - x\right)\left(c_{12}\,\bar{u} + c_{22}\,\bar{v}\right)}{\ell\left(c_{22}\,\ell^2 + 12c_{33}\right)}. \end{aligned} \tag{31}$$

References

1. Misra, A., Nejadsadeghi, N., De Angelo, M., Placidi, L.: Chiral metamaterial predicted by granular micromechanics: verified with 1D example synthesized using additive manufacturing. Contin. Mech. Thermodyn. **32**, 1497–1513 (2020)
2. De Angelo, M., Placidi, L., Nejadsadeghi, N., Misra, A.: Non-standard Timoshenko beam model for chiral metamaterial: identification of stiffness parameters. Mech. Res. Commun. **103**, 103462 (2020)
3. Nejadsadeghi, N., Hild, F., Misra, A.: Parametric experimentation to evaluate chiral bars representative of granular motif. Int. J. Mech. Sci. **221**, 107184 (2022)
4. Nejadsadeghi, N., De Angelo, M., Misra, A., Hild, F.: Multiscalar DIC analyses of granular string under stretch reveal non-standard deformation mechanisms. Int. J. Solids Struct. **239–240**, 111402 (2022)
5. Maconachie, T., Leary, M., Lozanovski, B., Zhang, X., Qian, M., Faruque, O., Brandt, M.: SLM lattice structures: properties, performance, applications and challenges. Mater. Des. **183**, 108137 (2019)
6. Nazir, A., Abate, K.M., Kumar, A., Jeng, J.: A state-of-the-art review on types, design, optimization, and additive manufacturing of cellular structures. Int. J. Adv. Manuf. Technol. **104**, 3489–3510 (2019)

7. dell'Isola, F., Seppecher, P., Spagnuolo, M., Barchiesi, E., Hild, F., Lekszycki, T., Giorgio, I., Placidi, L., Andreaus, U., Cuomo, M., et al.: Advances in pantographic structures: design, manufacturing, models, experiments and image analyses. Contin. Mech. Thermodyn. **31**, 1231–1282 (2019)
8. dell'Isola, F., Seppecher, P., Alibert, J.J., et al.: Pantographic metamaterials: an example of mathematically driven design and of its technological challenges. Contin. Mech. Thermodyn. **31**, 851–884 (2019)
9. Ciallella, A., Giorgio, I., Barchiesi, E., Alaimo, G., Cattenone, A., Smaniotto, B., Vintache, A., D'Annibale, F., dell'Isola, F., Hild, F., et al.: A 3D pantographic metamaterial behaving as a mechanical shield: experimental and numerical evidence. Mater. Des. **8**, 112554 (2023)
10. Borikar, G.P., Patil, A.R., Kolekar, S.B.: Additively manufactured lattice structures and materials: present progress and future scope. Int. J. Precis. Eng. Manuf. **24**, 2133–2180 (2023)
11. Barchiesi, E., Spagnuolo, M., Placidi, L.: Mechanical metamaterials: a state of the art. Math. Mech. Solids **24**, 212–234 (2019)
12. Casalotti, A., D'Annibale, F., Rosi, G.: Multi-scale design of an architected composite structure with optimized graded properties. Compos. Struct. **24**, 112608 (2020)
13. Carcaterra, A., dell'Isola, F., Esposito, R., Pulvirenti, M.: Macroscopic description of microscopically strongly inhomogenous systems: a mathematical basis for the synthesis of higher gradients metamaterials. Arch. Ration. Mech. Anal. **218**, 1239–1262 (2015)
14. Turco, E., Barchiesi, E., Giorgio, I., dell'Isola, F.: A Lagrangian Hencky-type non-linear model suitable for metamaterials design of shearable and extensible slender deformable bodies alternative to Timoshenko theory. Int. J. Non-Linear Mech. **123**, 103481 (2020)
15. Giorgio, I., Misra, A., Placidi, L.: Geometrically Nonlinear Cosserat Elasticity with Chiral Effects Based upon Granular Micromechanics, pp. 273–292 (2023)
16. Li, T., Li, Y.: Prediction of the anisotropy of chiral mechanical metamaterials via micropolar modeling. J. Appl. Mech. **89**, 101006 (2022)
17. Askari, M., Hutchins, D.A., Thomas, P.J., Astolfi, L., Watson, R.L., Abdi, M., Ricci, M., Laureti, S., Nie, L., Freear, S., Wildman, R., Tuck, C., Clarke, M., Woods, E., Clare, A.T.: Additive manufacturing of metamaterials: a review. Addit. Manuf. **36**, 101562 (2020)
18. Mizzi, L., Simonetti, A., Spaggiari, A.: Mechanical properties and failure modes of additively-manufactured chiral metamaterials based on Euclidean tessellations: an experimental and finite element study. Rapid Prototyp. J. **30**, 59–71 (2024)
19. Karathanasopoulos, N., Dos Reis, F., Diamantopoulou, M., Ganghoffer, J.-F.: Mechanics of beams made from chiral metamaterials: tuning deflections through normal-shear strain couplings. Mater. Des. **189**, 108520 (2020)
20. Giorgio, I., dell'Isola, F., Misra, A.: Chirality in 2D Cosserat media related to stretch-micro-rotation coupling with links to granular micromechanics. Int. J. Solids Struct. **202**, 28–38 (2020)
21. Ji, M., Cho, Y., Lee, S.-J., Park, K.: Design and analysis of three-dimensional chiral metamaterials for enhanced torsional compliance. Smart Mater. Struct. **33**, 045009 (2024)
22. Li, T., Li, Y.: Mechanical behaviors of three-dimensional chiral mechanical metamaterials. Compos. B Eng. **270**, 111141 (2024)
23. Lin, G., Li, J., Chen, P., Sun, W., Chizhik, S., Makhaniok, A., Melnikova, G., Kuznetsova, T.: Buckling of lattice columns made from three-dimensional chiral mechanical metamaterials. Int. J. Mech. Sci. **194**, 106208 (2021)
24. Stilz, M., Breuling, J., Eugster, S., Pawlikowski, M., Grygoruk, R.: Chirality effects in panto-cylindrical structures. Math. Mech. Solids **29**, 818–830 (2024)
25. Vangelatos, Z., Komvopoulos, K., Spanos, J., Farsari, M., Grigoropoulos, C.: Anisotropic and curved lattice members enhance the structural integrity and mechanical performance of architected metamaterials. Int. J. Solids Struct. **193–194**, 287–301 (2020)
26. Noor, A.K.: Continuum modeling for repetitive lattice structures. Appl. Mech. Rev. **41**, 285–296 (1988)
27. Tollenaere, H., Caillerie, D.: Continuous modeling of lattice structures by homogenization. Adv. Eng. Softw. **29**, 699–705 (1998)
28. Chesnais, C., Boutin, C., Hans, S.: In: Altenbach, H., Maugin, G., Erofeev, V., (eds.) Mechanics of Generalized Continua, pp. 57–76. Springer, Berlin (2011)
29. Turco, E.: In-plane shear loading of granular membranes modeled as a Lagrangian assembly of rotating elastic particles. Mech. Res. Commun. **92**, 61–66 (2018)
30. Pan, C., Han, Y., Lu, J.: Design and optimization of lattice structures: a review. Appl. Sci. **10**, 6374 (2020)
31. Somnic, J., Jo, B.W.: Status and challenges in homogenization methods for lattice materials. Materials **15**, 605 (2022)
32. D'Annibale, F., Ferretti, M., Luongo, A.: Static and dynamic responses of micro-structured beams. Appl. Sci. **10**, 6836 (2020)
33. Ferretti, M., D'Annibale, F., Luongo, A.: Modeling beam-like planar structures by a one-dimensional continuum: an analytical-numerical method. J. Appl. Comput. Mech. **7**, 1020–1033 (2021)
34. Ferretti, M., D'Annibale, F.: Buckling of planar micro-structured beams. Appl. Sci. **10**, 6506 (2020)
35. Luongo, A.: In: Challamel, N., Kaplunov, J., Takewaki, I., (eds.) Modern Trends in Structural and Solid Mechanics, pp. 143–165. ISTE-Wiley (2021)
36. Piccardo, G., Tubino, F., Luongo, A.: A shear-shear torsional beam model for nonlinear aeroelastic analysis of tower buildings. Z. Angew. Math. Phys. **66**, 1895–1913 (2015)
37. Piccardo, G., Tubino, F., Luongo, A.: Equivalent nonlinear beam model for the 3-D analysis of shear-type buildings: application to aeroelastic instability. Int. J. Non-Linear Mech. **80**, 52–65 (2016)
38. Piccardo, G., Tubino, F., Luongo, A.: Equivalent Timoshenko linear beam model for the static and dynamic analysis of tower buildings. Appl. Math. Model. **71**, 77–95 (2019)
39. Ferretti, M.: Flexural torsional buckling of uniformly compressed beam-like structures. Contin. Mech. Thermodyn. **30**, 977–993 (2018)

40. D'Annibale, F., Ferretti, M., Luongo, A.: Shear-shear-torsional homogenous beam models for nonlinear periodic beam-like structures. Eng. Struct. **184**, 115–133 (2019)
41. Di Nino, S., Luongo, A.: Nonlinear aeroelastic behavior of a base-isolated beam under steady wind flow. Int. J. Non-Linear Mech. **119**, 103340 (2020)
42. Ferretti, M., D'Annibale, F., Luongo, A.: Buckling of tower buildings on elastic foundation under compressive tip forces and self-weight. Contin. Mech. Thermodyn. **35**, 799–819 (2020)
43. Luongo, A., Zulli, D.: Free and forced linear dynamics of a homogeneous model for beam-like structures. Meccanica **55**, 907–925 (2020)
44. Luongo, A., D'Annibale, F., Ferretti, M.: Shear and flexural factors for static analysis of homogenized beam models of planar frames. Eng. Struct. **228**, 111440 (2021)
45. Chajes, M.J., Romstad, K.M., McCallen, D.B.: Analysis of multiple-bay frames using continuum model. J. Struct. Eng. **119**, 522–546 (1993)
46. Zalka, K.A.: Global Structural Analysis of Buildings. CRC Press, Boca Raton (2002)
47. Boutin, C., Hans, S.: Homogenisation of periodic discrete medium: application to dynamics of framed structures. Comput. Geotech. **30**, 303–320 (2003)
48. Hans, S., Boutin, C.: Dynamics of discrete framed structures: a unified homogenized description. J. Mech. Mater. Struct. **3**, 1709–1739 (2008)
49. Arabnejad, S., Pasini, D.: Mechanical properties of lattice materials via asymptotic homogenization and comparison with alternative homogenization methods. Int. J. Mech. Sci. **77**, 249–262 (2013)
50. Abali, B.E., Vazic, B., Newell, P.: Influence of microstructure on size effect for metamaterials applied in composite structures. Mech. Res. Commun. **122**, 103877 (2022)
51. Barchiesi, E.: Equilibria of axial-transversely loaded homogenized Duoskelion beams. Math. Mech. Complex Syst. **12**, 283–309 (2024)
52. Sun, C.T., Kim, B.J., Bogdanoff, J.L.: On the derivation of equivalent simple models for beam-and plate-like structures in dynamic analysis. In: Dynamics Specialists Conference, p. 624 (1981)
53. Healey, T.J.: Material symmetry and chirality in nonlinearly elastic rods. Math. Mech. Solids **7**, 405–420 (2002)
54. Calladine, C.R., Drew, H.: Understanding DNA: The Molecule and How It Works. Academic Press, Cambridge (1997)
55. Costello, G.A.: Theory of Wire Rope. Springer, Berlin (1997)
56. Barchiesi, E., dell'Isola, F., Seppecher, P., Turco, E.: A beam model for Duoskelion structures derived by asymptotic homogenization and its application to axial loading problems. Eur. J. Mech. A. Solids **98**, 104848 (2023)
57. Turco, E., Barchiesi, E., dell'Isola, F.: In-plane dynamic buckling of duoskelion beam-like structures: discrete modeling and numerical results. Math. Mech. Solids **27**, 1164–1184 (2022)
58. McAvoy, R., Barchiesi, E.: Towards the Galerkin approximation of tetraskelion metamaterials. Contin. Mech. Thermodyn. **37**, 6 (2025)
59. Giorgio, I., Hild, F., Gerami, E., dell'Isola, F., Misra, A.: Experimental verification of 2D Cosserat chirality with stretch-micro-rotation coupling in orthotropic metamaterials with granular motif. Mech. Res. Commun. **126**, 104020 (2022)
60. Abali, B.E., Barchiesi, E.: Additive manufacturing introduced substructure and computational determination of metamaterials parameters by means of the asymptotic homogenization. Contin. Mech. Thermodyn. **33**, 993–1009 (2021)
61. Antman, S.S.: Linear Theories of Elasticity and Thermoelasticity, pp. 641–703. Springer, Berlin (1973)
62. Antman, S.S.: Nonlinear Problems of Elasticity. Springer, Berlin (2005)
63. Luongo, A., Zulli, D.: Mathematical Models of Beams and Cables. Wiley, New York (2013)
64. Elishakoff, I.: Who developed the so-called Timoshenko beam theory? Math. Mech. Solids **25**, 97–116 (2020)